

NACA RM L56H22a

UNCLASSIFIED

CONFIDENTIAL

Copy 6  
RM L56H22a

C.2



# RESEARCH MEMORANDUM

WIND-TUNNEL INVESTIGATION OF TWO  
VERTICAL-TAKE-OFF-AND-LANDING JET BOMBER AIRPLANE  
CONFIGURATIONS AT MACH NUMBERS OF 1.94 AND 2.40

By Robert A. Jones and Robert W. Rainey

Langley Aeronautical Laboratory  
Langley Field, Va.

CLASSIFICATION CHANGED

**LIBRARY COPY**

NOV 1 1956

LANGLEY AERONAUTICAL LABORATORY  
LIBRARY, NACA  
LANGLEY FIELD, VIRGINIA

Authority of TPA #39 Date Jan 13 1957  
CLASSIFIED DOCUMENT

This material contains information affecting the National Defense of the United States within the meaning of the espionage laws, Title 18, U.S.C., Secs. 793 and 794, the transmission or revelation of which in any manner to an unauthorized person is prohibited by law.

## NATIONAL ADVISORY COMMITTEE FOR AERONAUTICS

WASHINGTON

October 31, 1956

CONFIDENTIAL

UNCLASSIFIED



## NATIONAL ADVISORY COMMITTEE FOR AERONAUTICS

## RESEARCH MEMORANDUM

WIND-TUNNEL INVESTIGATION OF TWO  
VERTICAL-TAKE-OFF-AND-LANDING JET BOMBER AIRPLANE  
CONFIGURATIONS AT MACH NUMBERS OF 1.94 AND 2.40

By Robert A. Jones and Robert W. Rainey

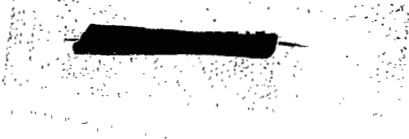
## SUMMARY

An investigation has been conducted in the Langley 9-inch supersonic tunnel to obtain some insight into the basic aerodynamic characteristics of two vertical-take-off-and-landing jet bomber airplanes, one having a high wing, the other having a low wing. The wings had an aspect ratio of 1.067 and had open leading and trailing edges to represent the inlets and exits of a multiple-engine installation within the wings. Jet flow was not simulated. The fuselage of each model had a fineness ratio of 15.0. The tests of these configurations were made at Mach numbers of 1.94 and 2.40, with and without transition strips installed on the models, to determine lift-drag ratios, static longitudinal and directional stability, and the effects of the location and incidence angle of the horizontal tail upon lift-drag ratio and longitudinal stability. These tests were made through an angle-of-attack range at a yaw angle of  $0^\circ$  and through an angle-of-yaw range at an angle of attack of  $0^\circ$ .

The high-tail configurations had higher lift-drag ratios with maximums of about 4, wing internal drag being deducted. The horizontal-tail effectiveness was reduced when the tail was located in the region ahead of or occupied by the wing trailing-edge shock wave or in the region of the wing wake. The vertical tail of the low-wing model provided more directional stability than did the combination of the ventral and dorsal vertical tails of the high-wing model.

## INTRODUCTION

Some of the existing and proposed turbojet engines have geometric and performance characteristics that make them suitable for powering large vertical-take-off-and-landing (herein designated VTOL) aircraft which would be capable of cruising at supersonic speeds. The range that such an aircraft might have at Mach numbers of the order of 2 to 2.5



would be undesirably short, however, unless lift-drag ratios of the order of 3 to 4 could be realized.

In order to obtain an indication of the aerodynamic characteristics of two configurations envisioned to be supersonic-cruising VTOL aircraft, a preliminary investigation has been conducted in the Langley 9-inch supersonic tunnel. The tests of this investigation were made at Mach numbers of 1.94 and 2.40, with and without transition strips installed on the models, to determine lift-drag ratios, static longitudinal and directional stability, and the effects of the location and incidence angle of the horizontal tail upon the lift-drag ratio and longitudinal stability.

The fuselage of each model had a fineness ratio of 15.0 and the wing of each model had an aspect ratio of 1.067. The engines were assumed to be submerged within the wing. No jet flow was simulated and, therefore, the effects of jet interference were not obtained in the present tests.

#### SYMBOLS

$c$  wing chord, in.

$C_c$  cross-wind coefficient,  $\frac{\text{Cross-wind force}}{q_\infty S}$

$C_D$  drag coefficient,  $\frac{\text{Drag}}{q_\infty S}$

$C_{D,p}$  wing internal pressure drag coefficient,  $\frac{\text{Internal drag}}{q_\infty S}$

$C_L$  lift coefficient,  $\frac{\text{Lift}}{q_\infty S}$

$C_{m,w}$  pitching-moment coefficient (referenced to 45 percent wing chord, see fig. 2),  $\frac{\text{Pitching moment}}{q_\infty S c}$

$C_{n,w}$  yawing-moment coefficient (referenced to 45 percent wing chord, see fig. 2) (Note that the yawing moment has been referred to wing chord rather than to wing span),  $\frac{\text{Yawing moment}}{q_\infty S c}$

$\frac{dC_m}{dC_L}$	stability parameter
$h$	horizontal-tail height measured from wing center line, in.
$i_t$	tail incidence angle, deg
$L/D$	lift-drag ratio
$M$	Mach number
$q$	dynamic pressure, lb/sq ft
$r$	fuselage radius, in.
$R$	Reynolds number, based on wing chord
$S$	wing area, including portion submerged in fuselage, sq in.
$x$	distance along fuselage measured from nose, in.
$x_{ac}$	distance from wing leading edge to aerodynamic-center location, in.
$x_{cg}$	distance from wing leading edge to center of gravity, in.
$x_{cp}$	distance from wing leading edge to center-of-pressure location, in.
$\alpha$	angle of attack, deg
$\beta$	angle of sideslip, deg
$\epsilon$	effective downwash angle; that horizontal tail angle, relative to free stream, which would result in no horizontal tail contribution to lift, deg

## Subscripts:

$\infty$	free stream
$w$	with respect to wind axis

## APPARATUS AND MODELS

## Wind Tunnel

All tests were made in the Langley 9-inch supersonic tunnel which is a continuous-operation complete-return type of tunnel in which the absolute stagnation pressure may be varied and controlled from about 1/10 atmosphere to about 4 atmospheres. The stagnation temperature and dewpoint may also be varied and controlled. The Mach number is varied by interchanging nozzle blocks which form test sections approximately 9 inches square.

## Models

Photographs of the two basic models without transition strips are presented in figure 1 and drawings of these models showing the locations of the transition strips are presented in figure 2. Figure 3 shows the various locations and incidence angles of the horizontal tails that were investigated. Some additional pertinent dimensions and parameters are presented in table I. All models were constructed of metal, and all surfaces were finished smooth.

Fuselages.- The fuselages had a fineness ratio of 15.0. The basic fuselage consisted of a closed parabolic arc of revolution determined by the equation  $r = 0.133x - 0.0133x^2$  where  $r$  is the radius and  $x$  is the distance along the axis measured from the nose. This contour was modified near the rear of the fuselage to accommodate the sting. (See fig. 2.) For model 1, the afterbody was modified to a frustrum of a right cone which converged symmetrically about the fuselage center line and was tangent to the parabolic arc of revolution at a distance of 6.50 inches from the nose. For model 2, the afterbody did not converge symmetrically as did model 1 but was swept up such that the meridian along the top of the body was a straight line from the maximum diameter rearward. The stings on all models were integral parts of the fuselage.

Wings.- The wings on both models had the same rectangular plan form and aspect ratio; the only difference was in their vertical location (fig. 2), model 1 having a high wing and model 2 having a low wing. All wings were constructed of 1/32-inch steel sheet contoured on the external surfaces to be sharp at the leading and trailing edges and fastened to the body at an angle of incidence of  $0^\circ$ . As shown in figure 2, the wings were hollow with the gap between the upper and lower surfaces extending through the wing and over the entire wing span except for the region occupied by the body. There were thus no mechanical obstructions to passage of air through the wing. In order to obtain an idea of the pressures and flow within the wing, the wing on a replica of model 1, without

tails, was instrumented internally with 18 pressure orifices along a chordwise station midway of the semispan of the wing. The orifices were located 1/4 inch apart, nine on the upper surface and nine on the lower.

Canopies.- The canopies were made of steel and as nearly identical as possible. The windshields of the canopies were flat and the fuselage-windshield junctures were located at a station 7.5 percent of the body length from the nose.

Tails.- All vertical and horizontal tails were made from 1/32-inch steel sheet and were sharpened on the leading and trailing edges. The dimensions of the horizontal tail were the same on both models, and the vertical positions and incidence angles were set as indicated in figure 3. Model 1 had a ventral fin whereas model 2 did not; however, the total exposed vertical-tail area was the same on both models.

Transition strips.- Transition strips were installed only on model 1 with the low tail and model 2 with the high tail. The locations of the transition strips are shown in figure 2. The strips were 1/8 inch wide and about 0.006 inch thick and consisted of fairly evenly distributed aluminum-oxide crystals (ref. 1).

#### Model Installation

The models were sting mounted to the model support of the external balance system. The sting was shielded by a movable windshield. (See fig. 1(a).) The gap between the model base and the snout of the windshield was about 0.020 inch for all tests. A 1/16-inch-diameter mirror was flush mounted in the fuselage just rearward of the wing of the model for use with an optical angle-of-attack system.

#### Balance System

The balance used in these tests is a six-component, external type which utilizes mechanical self-balancing beams for force measurements; however, during the present tests, only three components were measured. Sideslip measurements were obtained by rotating the model 90° relative to the balance. A detailed description of the balance system is given in the appendix of reference 2.

#### TESTS

The tests were conducted at Mach numbers of 1.94 and 2.40 and Reynolds numbers of  $0.80 \times 10^6$  and  $0.64 \times 10^6$ , respectively, based on

the wing chord. Some of these tests were made with transition strips installed on the models; for the tests with transition strips the effective Reynolds number was considerably higher. Corrections, which have been standardized and considered routine for all sting-mounted model tests in the Langley 9-inch supersonic tunnel, were applied to the drags of each model to account for the difference between the free-stream static pressure and the measured pressure in the windshield and balance-box enclosure.

### PRECISION

The accuracy of angle of attack and of tail incidence angle was  $\pm 0.1^\circ$  and  $\pm 0.25^\circ$ , respectively. The estimated errors in the other measured quantities are listed below.

Quantity	Estimated error for -	
	$M_\infty = 1.94$	$M_\infty = 2.40$
Mach number . . . . .	$\pm 0.01$	$\pm 0.015$
Reynolds number . . . . .	$\pm 0.03 \times 10^6$	$\pm 0.03 \times 10^6$
Lift coefficient . . . . .	$\pm 0.0008$	$\pm 0.0010$
Drag coefficient . . . . .	$\pm 0.0006$	$\pm 0.0008$
Cross-wind coefficient . . . . .	$\pm 0.0010$	$\pm 0.0010$
Pitching-moment coefficient . . . . .	$\pm 0.0004$	$\pm 0.0006$
Yawing-moment coefficient . . . . .	$\pm 0.0004$	$\pm 0.0006$

### PRESENTATION OF RESULTS

The measured aerodynamic characteristics are presented in the following table:

Model	Tail configuration	Characteristic	Figure
1	High tail	Pitching	4
1	Low tail	Pitching	5
1	No horizontal tail	Pitching	6
1	Low tail	Sideslipping	7
2	High tail	Pitching	8
2	Low tail	Pitching	9
2	No horizontal tail	Pitching	10
2	High tail	Sideslipping	11

The incremental lift, pitching moment, and drag coefficients which resulted from adding the horizontal tail at  $i_t \approx 0^\circ$  are presented in figure 12. In figure 13 is presented the variation of effective downwash angle for the various configurations. In figure 14 are presented the aerodynamic-center locations of the configurations in pitch. A summary of lift-drag ratios is presented in figure 15. The center-of-pressure and aerodynamic-center locations of configurations in sideslip are presented in figure 16. Schlieren photographs of the models (without transition strips) are presented in figure 17.

## DISCUSSION

### Results in Pitch

Transition strips.- The results in pitch indicate that, in general, the addition of transition strips had little effect upon  $C_L$ ,  $C_D$ , and  $C_{m,w}$ . It appears probable, therefore, that for the models without transition strips the canopy-body and wing-body junctions caused natural transition to occur.

At  $M_\infty = 2.40$  the pitching moment of model 1, low tail,  $i_t = 0^\circ$ , (fig. 5(b)) was made slightly more negative by the addition of transition strips for angles of attack above  $6^\circ$ . It is believed that, at these angles of attack, the horizontal tail was located in the wake of the wing and that the separation point on the exterior surfaces of the wing was moved rearward by the artificially induced turbulent boundary layer; thus, the wake was thinner and the tail, more effective.

Internal wing drag.- The values of wing internal-pressure drag  $C_{D,p}$ , shown in figure 5, were determined by integrating the chordwise pressure distributions of the internal surfaces of the wing and by assuming them to be constant along the span and to be the same for both models. Thus, although the values of  $C_{D,p}$  are only crude estimates, they are very likely conservative. The internal skin-friction drag was calculated on the basis of a laminar boundary layer and with the assumption of free-stream Mach number within the wing. This drag estimate is therefore low and insures that the values of the lift-drag ratio  $L/D$  with the internal drag deducted are not optimistic. The calculated values of internal skin-friction drag coefficient were 0.0042 and 0.0047 at Mach numbers of 1.94 and 2.40, respectively. Lifts and pitching moments due to the internal wing pressure distribution and skin friction were negligible.

Longitudinal characteristics.- The variations of pitching moment with angle of attack of the horizontal-tail-off configurations of both models were essentially linear and had about the same slope. (See figs. 6 and 10.) Of the configurations with the horizontal tail on, it was noted



that at  $M_\infty = 1.94$  the pitching-moment coefficients and their variations with  $\alpha$  are similar for model 1, high tail (fig. 4) and for model 2, low tail (fig. 9). This result indicates that the horizontal-tail contributions of the two configurations were about equal (fig. 12) and that the flow fields which they occupied (behind the wing-trailing-edge shock waves) were similar. In addition, since the vertical locations of the two horizontal tails relative to the wing differed by only 0.11c, it is believed that the wing was the predominant source of interference. In figure 14 the similarity of the aerodynamic-center variation with angle of attack of these two configurations can be seen. These aforementioned similarities obviously do not take into account the effects of jet flow, although the effects of the flow through the wing were probably more in the direction of jet-flow effects than the effects of a blunt base with no jet.

The pitching-moment curve of model 2, high tail, is considerably different for the two Mach numbers (fig. 8). The primary difference is a region of reduced stability in the low lift range at  $M_\infty = 2.40$ . Schlieren photographs (fig. 17) show that at  $M_\infty = 2.40$  the high tail of model 2 is ahead of the wing-trailing-edge shock wave at low angles of attack, whereas at  $M_\infty = 1.94$  the same tail is behind this shock wave. The region of reduced stability at  $M_\infty = 2.40$  is probably the result of a higher effective downwash angle (fig. 13) because of the wing-tail interference when the tail is ahead of the trailing-edge shock wave. When this shock wave intersected the lower surface of the horizontal tail ( $\alpha \approx 2^\circ$ ), the upper tail surface was still subjected to the downwash although offset somewhat by the pressure rise across the shock wave and the reflected shock wave acting on the lower surface. As this shock wave progressed forward on the horizontal tail, the lift and negative pitching-moment increments increased (fig. 12), the effective downwash decreased (fig. 13), and the configuration became more stable. This condition caused a rearward movement of the aerodynamic-center location at an angle of attack of about  $2^\circ$  (fig. 14). The effect of a tail incidence angle of  $-5^\circ$  was to delay this rearward movement until an angle of attack of about  $4^\circ$ .

The small contribution of the low tail of model 1 to lift and pitching moment (fig. 12) is believed to be the result of the horizontal tail being subjected to the wing wake between angles of attack from  $4^\circ$  to  $8^\circ$  (fig. 17). In this angle-of-attack range the horizontal tail would, of course, be subject to jet interference. The reduction of the negative  $\Delta C_{m,w}$  of model 1, high tail (fig. 12(a)), at an angle of attack greater than about  $7^\circ$  is also believed to be the result of the wing wake.

Lift-drag ratios.— A summary of the lift-drag ratios is presented in figure 15. The values of  $L/D$ , internal drag being deducted, take into account the crude but conservative estimates of both the pressure

drag and the skin-friction drag discussed previously. Without the internal drag deducted, the high-tail configurations had higher lift-drag ratios than the low-tail configurations. With the internal drag deducted, the maximum lift-drag ratio values of the high-tail configurations were of the order of 4 for both models.

In order to compare the lift-drag ratios of the models at cruising conditions, the airplane weight was assumed to be 65,000 pounds; the gross weight, 175,000 pounds; and the altitude, 55,000 feet. In addition, it was assumed that the stability parameter  $dc_m/dc_L$  was -0.05 and that the change in  $C_L$  and  $C_m$  with tail incidence angle was linear. On the basis of these assumptions, the trim  $C_L$  was calculated to be 0.22 and the trim values of  $L/D$ ,  $\alpha$ ,  $i_t$ , and  $x_{cg}/c$  were as follows:

Model	Tail location	Mach number	$\alpha$ , deg	$i_t$ , deg	$\frac{x_{cg}}{c}$	$\frac{L}{D}$	$\frac{h}{c}$
1	High	1.94	6.0	-3.0	0.22	3.08	0.288
1	Low	1.94	5.9	0.3	.27	3.06	.126
2	High	1.94	5.5	-3.1	.45	3.22	.564
2	Low	1.94	5.7	-2.0	.32	3.17	.402
1	High	2.40	6.3	-2.6	.34	3.42	.288
1	Low	2.40	6.6	-1.0	.31	3.27	.126
2	High	2.40	5.5	4.0	.71	3.59	.564
2	Low	2.40	6.7	-4.0	.33	3.32	.402

For the values of  $L/D$  shown in the table, the internal drags have not been subtracted from the measured drag values. In each case the high-tail configurations had the higher  $L/D$  values and also required a more negative tail-incidence angle for trim with the exception of model 2, high tail, which was subject to the high downwash discussed earlier. It is of interest to note that for both Mach numbers the lift-drag ratio at trim increased as the tail height  $h/c$  increased from 0.126 to 0.564 with one exception. This exception (model 2, low tail,  $M_\infty = 2.40$ ) appears to be the result of the influence of the wing wake on the horizontal tail coupled with the high negative tail-incidence angle and large trim angle of attack. For a given model the lift-drag ratio at trim always increased with tail height.

#### Results in Sideslip

Sideslip results were obtained for two configurations at an angle of attack of  $0^\circ$ : model 1 with the low tail, and model 2 with the high tail. The variation of  $C_n$  with  $\beta$  of model 1, low tail, (fig. 7) is

more nonlinear and less stable than that of model 2, high tail (fig. 11). It is believed that the lower directional stability of model 1, low tail, is caused primarily by a large portion of the dorsal tail being submerged within the wake of the wing. (See fig. 17.) For model 2 none of the vertical tail is immersed in the wake of the wing.

### CONCLUSIONS

An investigation was made of two vertical-take-off-and-landing jet bomber airplanes (high wing and low wing) at Mach numbers of 1.94 and 2.40. Tests were made through an angle-of-attack range at an angle of yaw of  $0^\circ$  and through an angle-of-yaw range at an angle of attack of  $0^\circ$ . The bodies had a fineness ratio of 15.0 and the wings, an aspect ratio of 1.067. The engines were assumed to be submerged within the wings. Jet flow was not simulated. The results of the investigation indicated that:

1. The high-tail configurations had higher lift-drag ratios with maximums of about 4 for both the high- and low-wing models, wing internal drag being deducted.
2. The horizontal-tail effectiveness was reduced when the tail was located in region ahead of or occupied by the wing trailing-edge shock wave or in the region of the wing wake.
3. The vertical tail of the low-wing model provided more directional stability than did the combination of the ventral and dorsal tails of the high-wing model. This result was attributed to the effect of the wing wake on the dorsal vertical tail of the high-wing model.

Langley Aeronautical Laboratory,  
National Advisory Committee for Aeronautics,  
Langley Field, Va., August 8, 1956.

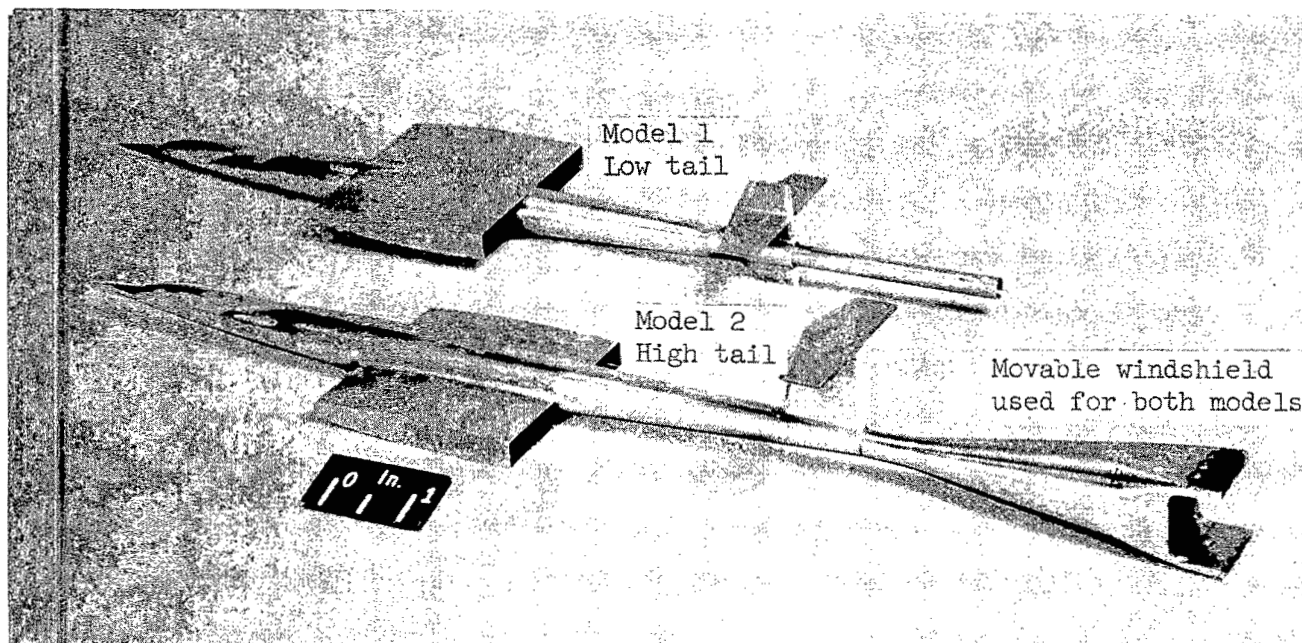
## REFERENCES

1. Fallis, William B.: On Distributed Roughness as a Means of Fixing Transition at High Supersonic Speeds. Jour. Aero. Sci. (Readers Forum), vol. 22, no. 5, May 1955, p. 339.
2. Rainey, Robert W.: Investigation of the Effects of Bomb-Bay Configuration Upon the Aerodynamic Characteristics of a Body With Circular Cross Section at Supersonic Speeds. NACA RM L55E27, 1955.

TABLE I

## DESIGN MODEL DIMENSIONS AND PARAMETERS

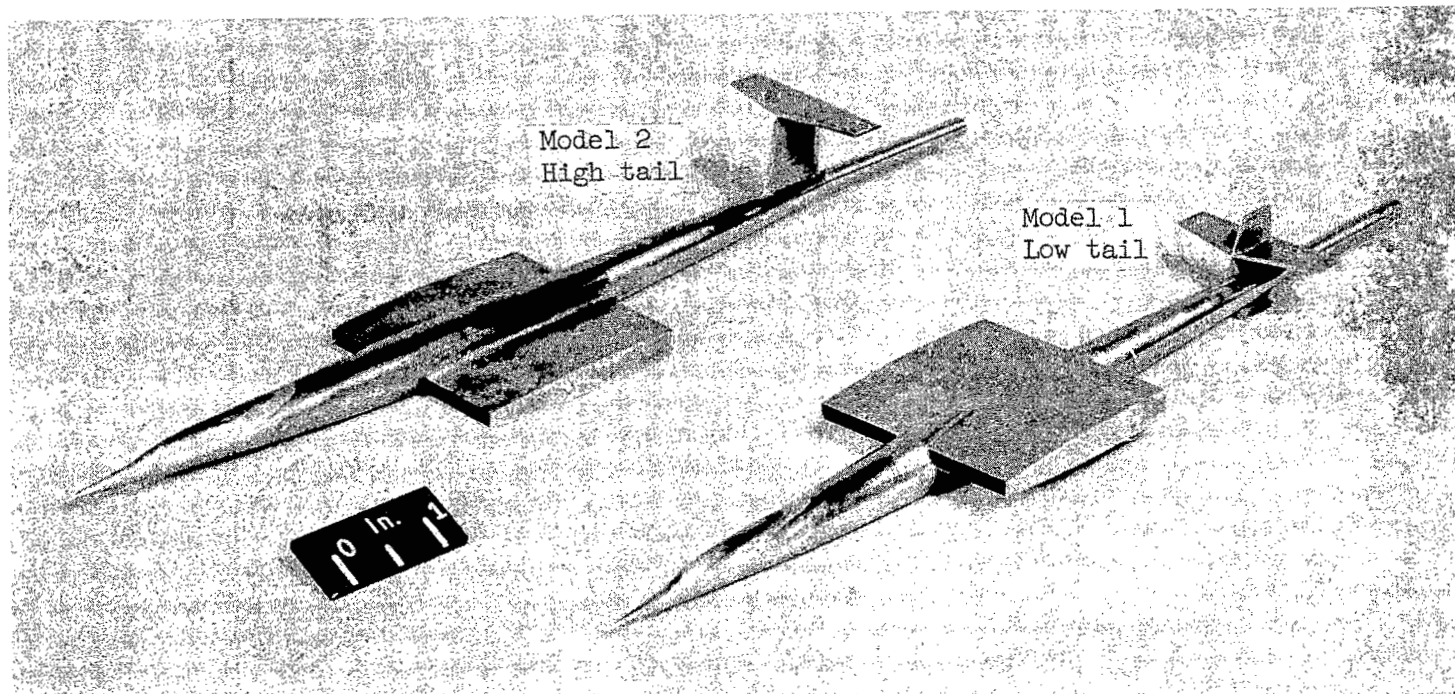
Components	Model 1	Model 2
<b>Fuselage:</b>		
Length, in. . . . .	10.000	10.000
Fineness ratio . . . . .	15.0	15.0
Maximum diameter, in. . . . .	0.667	0.667
Center of gravity, percent length . . . . .	51.25	51.25
Wing leading edge rearward of nose, in. . . . .	4.000	4.000
Base diameter, in. . . . .	0.300	0.310
Sting diameter, in. . . . .	0.250	0.250
<b>Wing:</b>		
Total area, sq in. . . . .	6.665	6.665
Chord, in. . . . .	2.500	2.500
Span, in. . . . .	2.668	2.668
Aspect ratio . . . . .	1.067	1.067
Model center of gravity, percent chord . . . . .	45.0	45.0
<b>Horizontal tail:</b>		
Span, in. . . . .	2.082	2.082
Root chord, in. . . . .	0.750	0.750
Tip chord, in. . . . .	0.500	0.500
Aspect ratio . . . . .	1.666	1.666
Area, sq in. . . . .	1.312	1.312
<b>Vertical tail:</b>		
<b>Ventral tail:</b>		
Tip chord, in. . . . .	0.533	None
Root chord, in. . . . .	0.802	None
Chord at fuselage center line, in. . . . .	1.000	None
<b>Dorsal tail:</b>		
Tip chord, in. . . . .	0.533	0.750
Root chord, in. . . . .	0.902	0.902
Chord at fuselage center line, in. . . . .	1.000	1.033
Exposed area, sq in. . . . .	0.760	0.760



(a) Upper rear three-quarter view.

L-92662.1

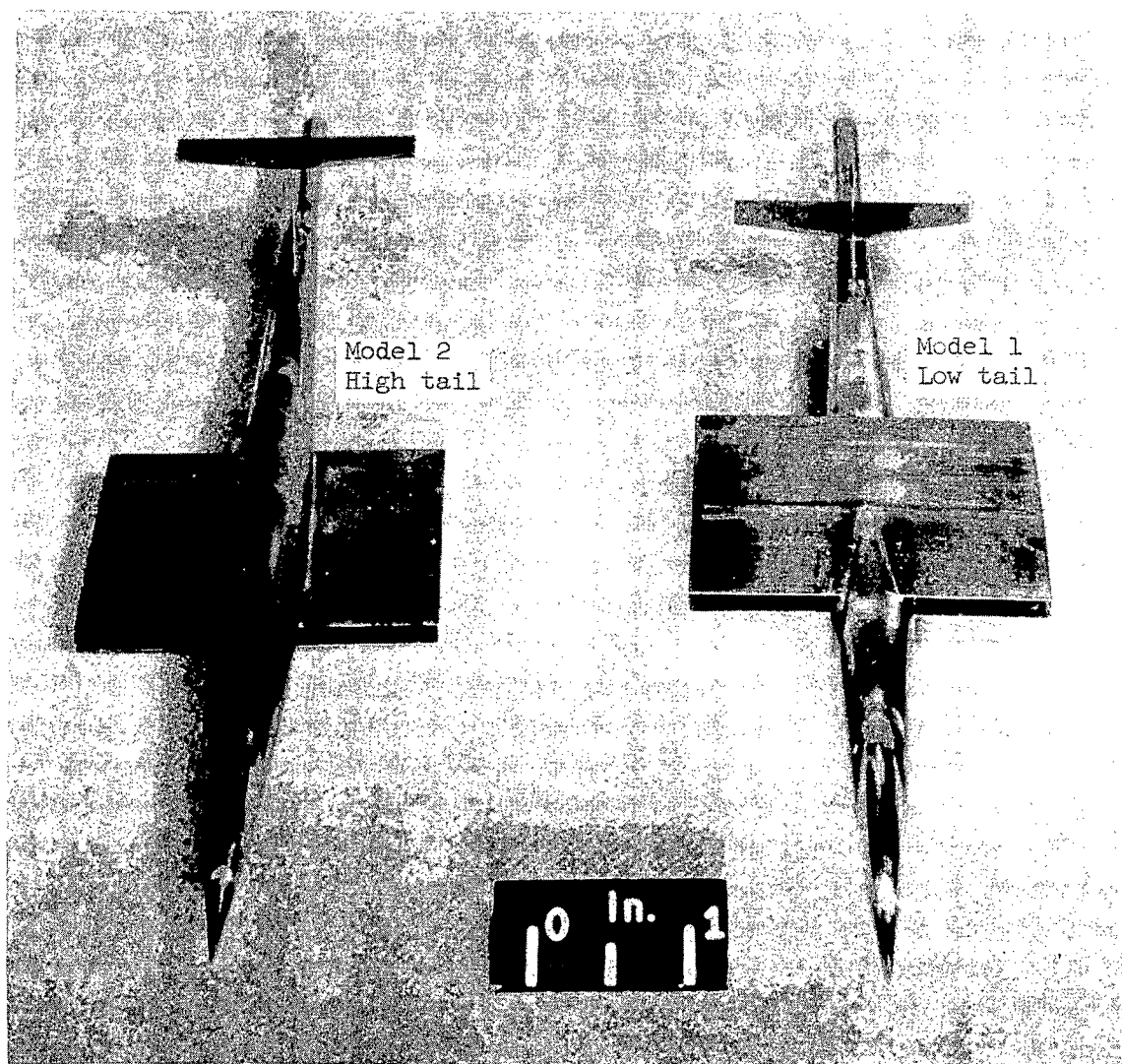
Figure 1.- Model photographs.



(b) Upper front three-quarter view.

L-92663.1

Figure 1.- Continued.

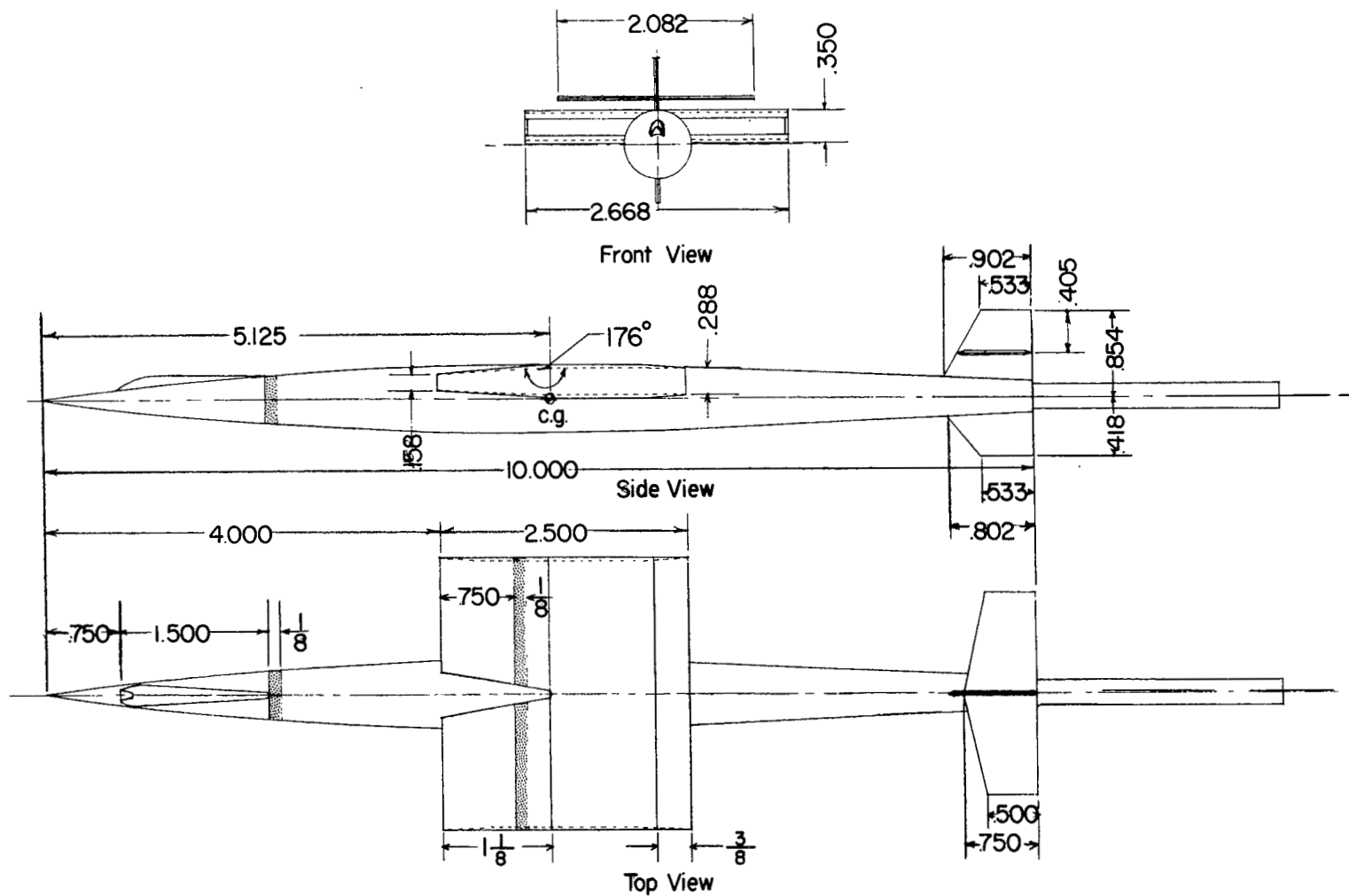


(c) Upper front view.

L-92664.1

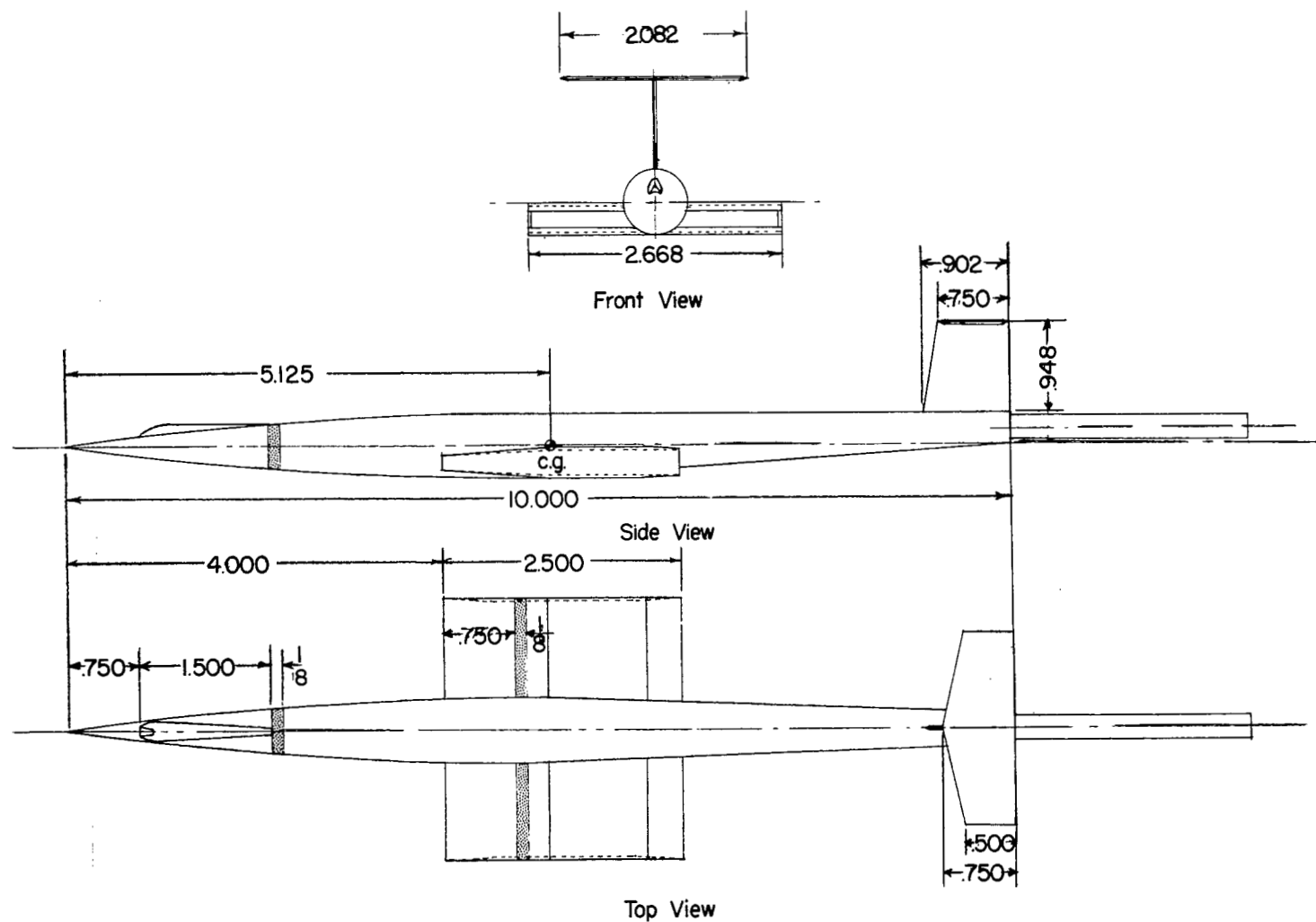
Figure 1.- Concluded.





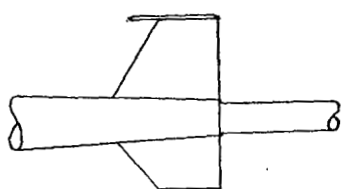
(a) Model 1, low tail.

Figure 2.- Three-view drawing of models.

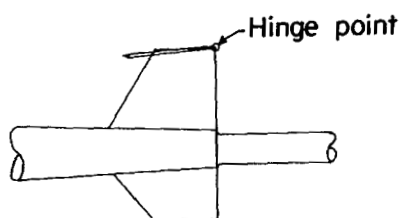
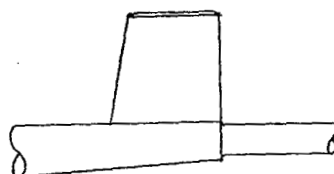


(b) Model 2, high tail.

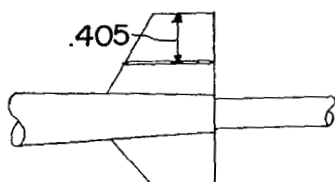
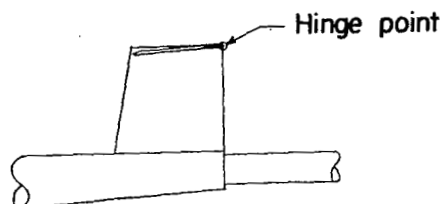
Figure 2.- Concluded.



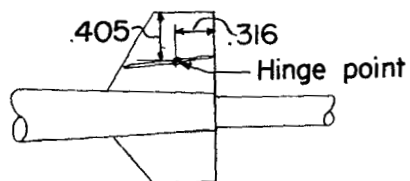
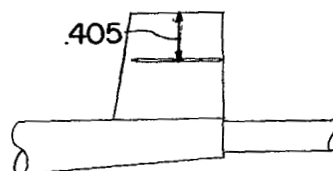
High tail  
 $i_t \approx 0^\circ$



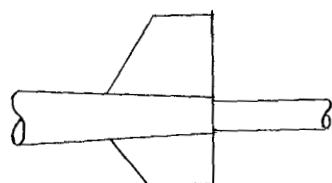
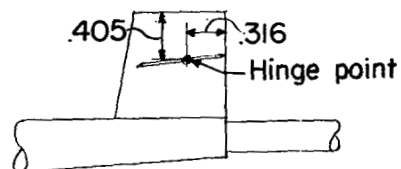
High tail  
 $i_t \approx -5^\circ$



Low tail  
 $i_t \approx 0^\circ$

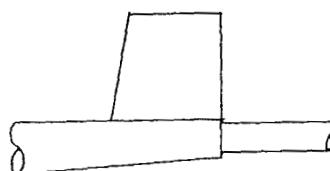


Low tail  
 $i_t \approx -5^\circ$



Model 1

No horizontal tail



Model 2

Figure 3.- Horizontal-tail locations.

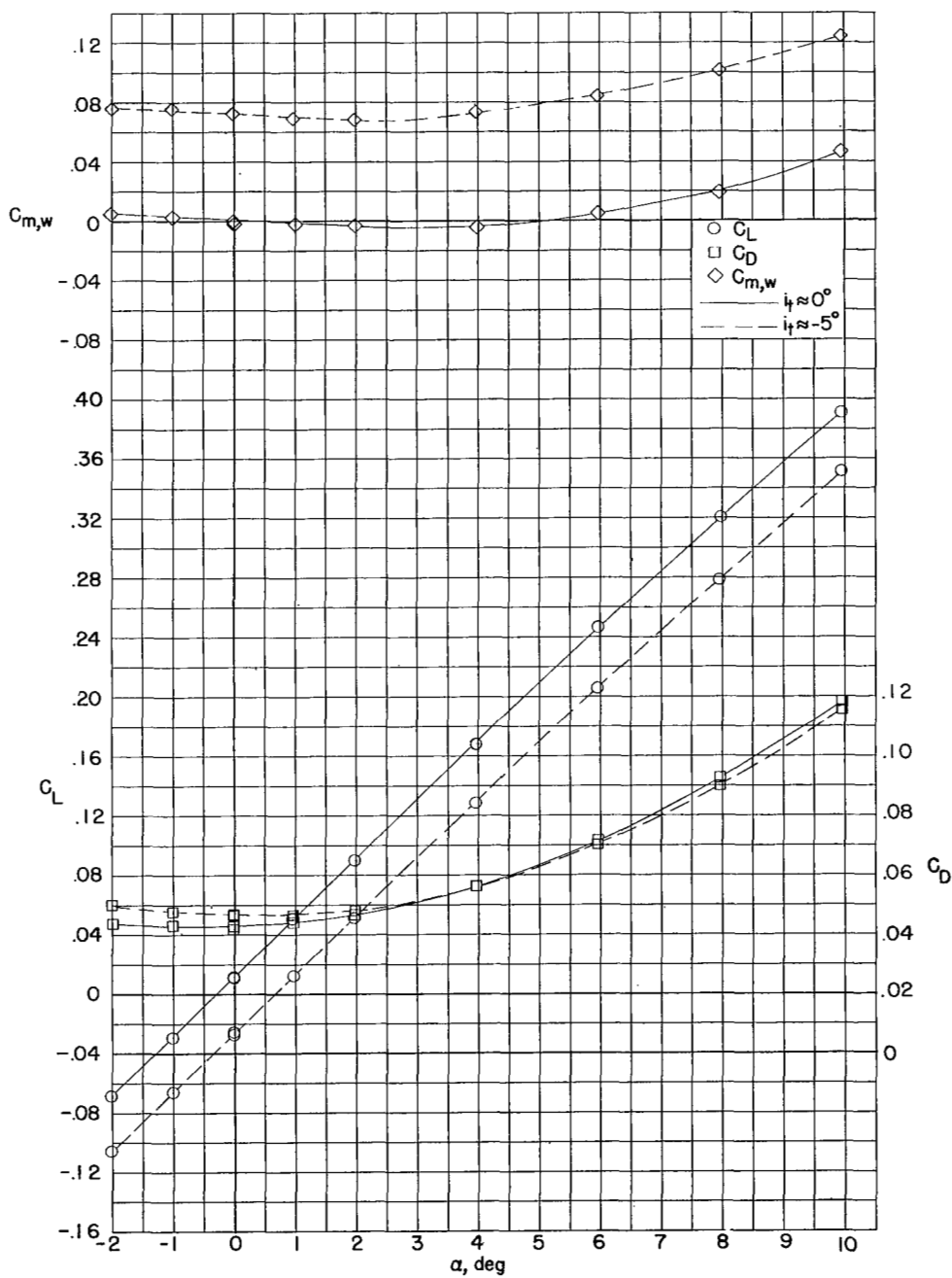
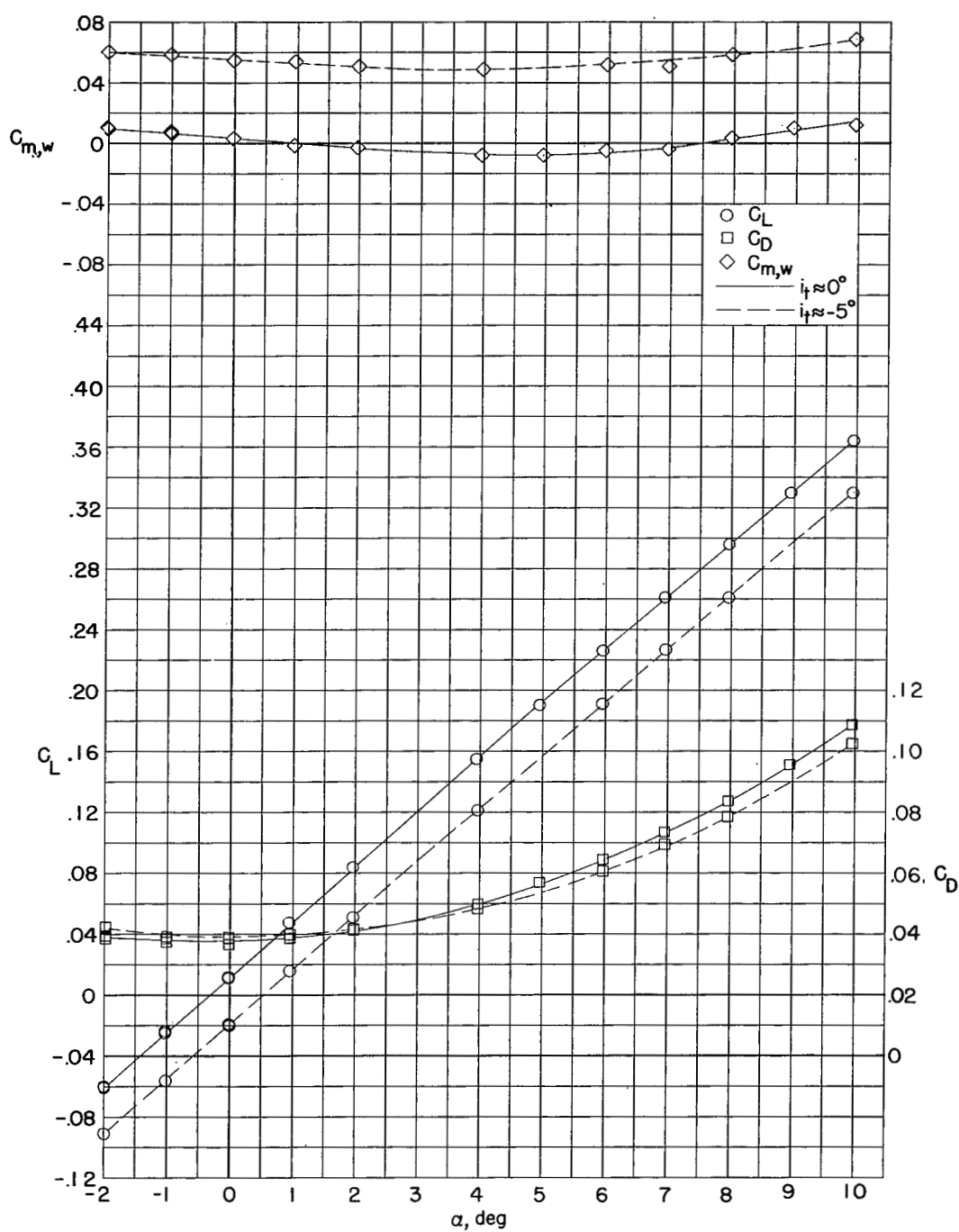
(a)  $M_\infty = 1.94$ .

Figure 4.- Measured aerodynamic characteristics of model 1 high-tail configuration in pitch.



(b)  $M_\infty = 2.40$ .

Figure 4.- Concluded.

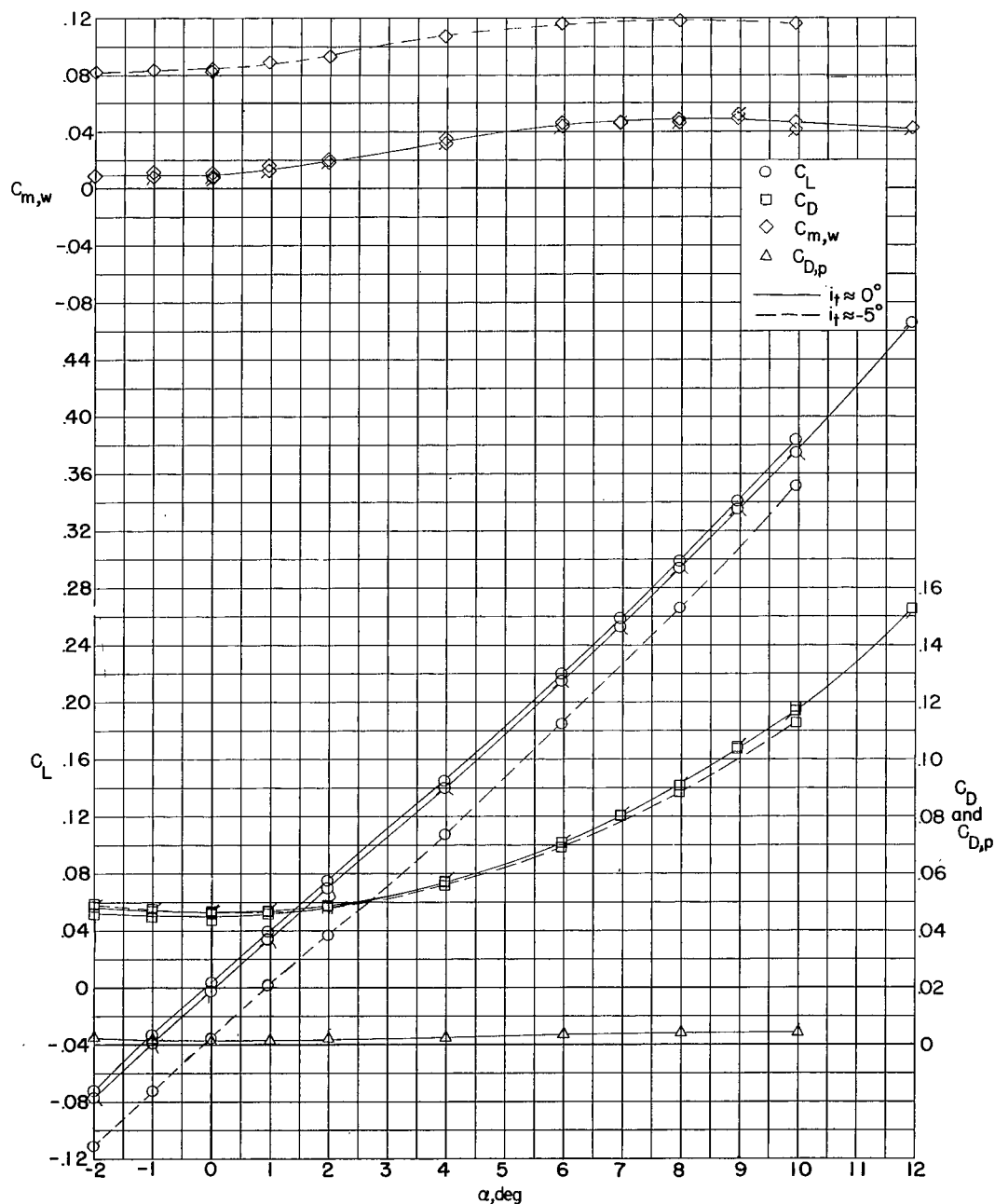
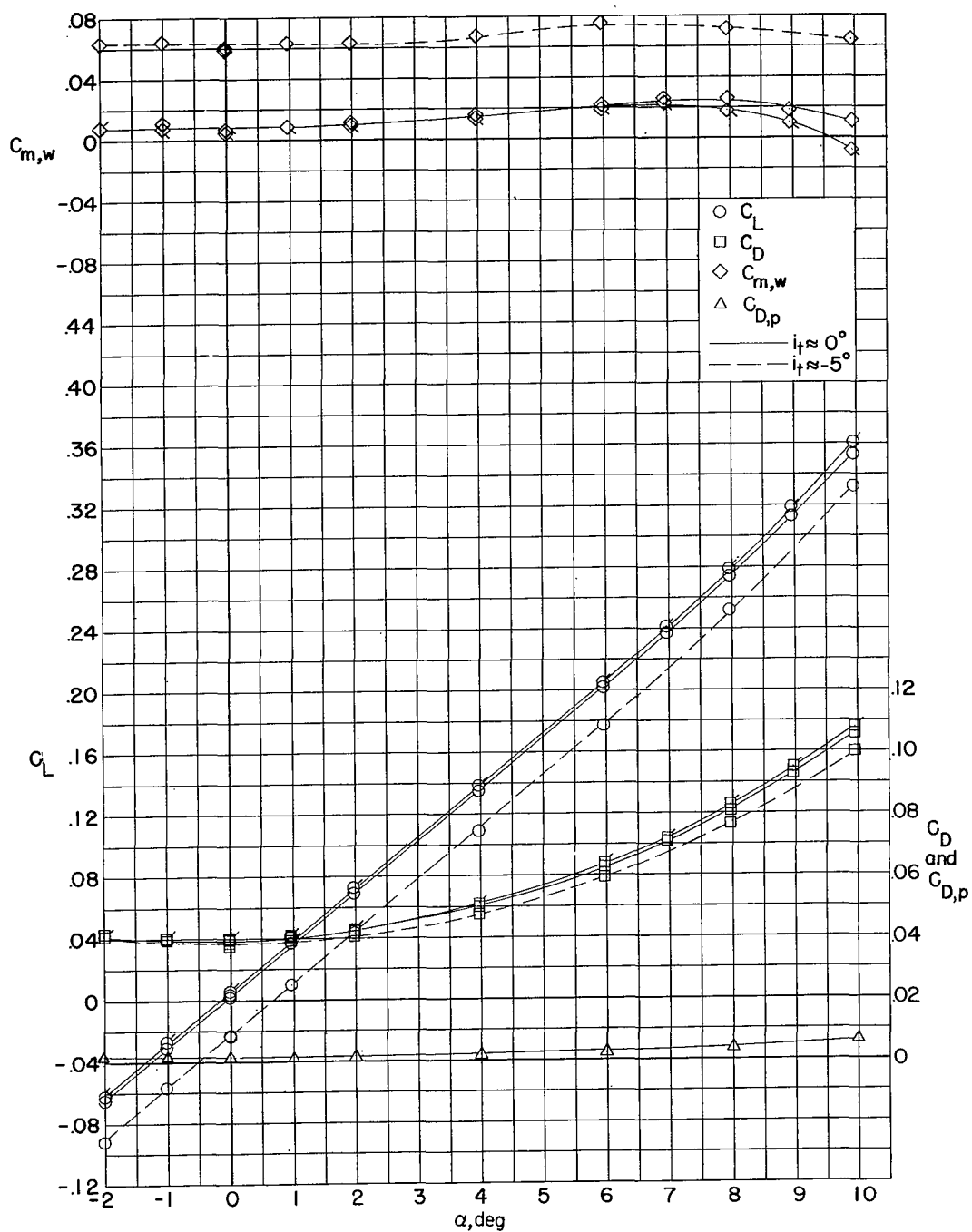
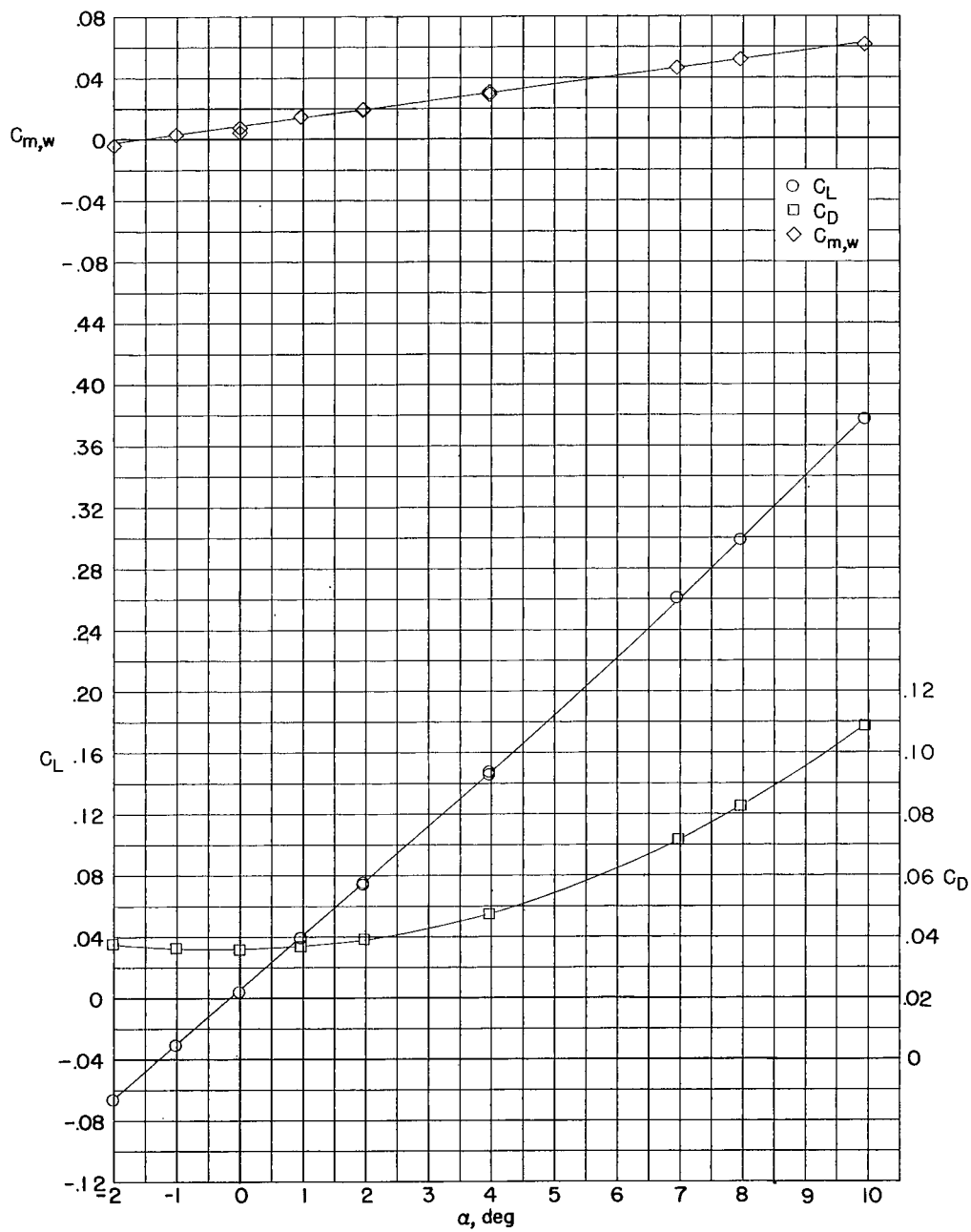
(a)  $M_\infty = 1.94$ .

Figure 5.- Measured aerodynamic characteristics of model 1 low-tail configuration in pitch. (Flagged symbols indicate model with transition strips.)



(b)  $M_\infty = 2.40$ .

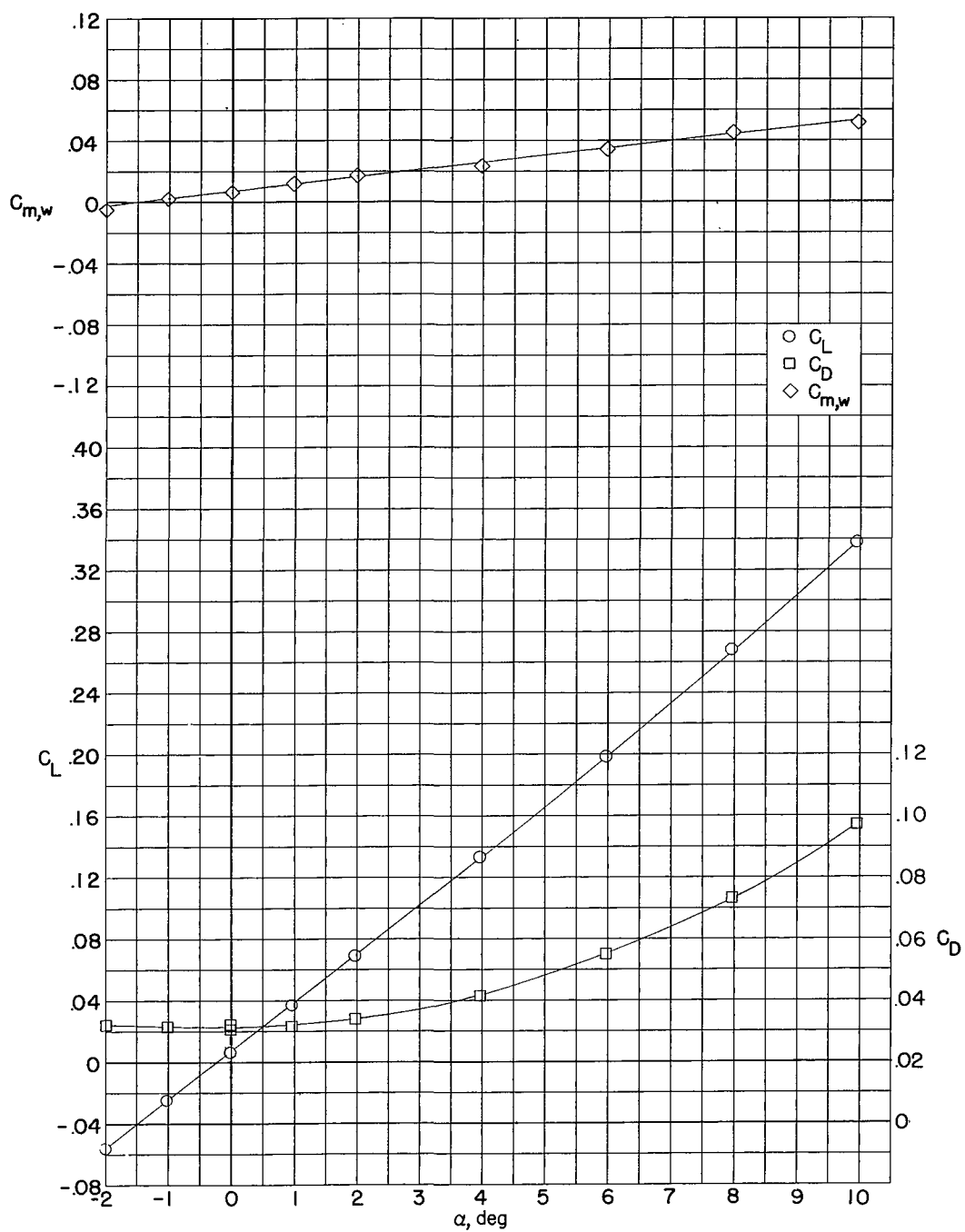
Figure 5.- Concluded.



(a)  $M_\infty = 1.94$ .

Figure 6.- Measured aerodynamic characteristics of model 1 in pitch.  
No horizontal tail.





(b)  $M_\infty = 2.40$ .

Figure 6.- Concluded.

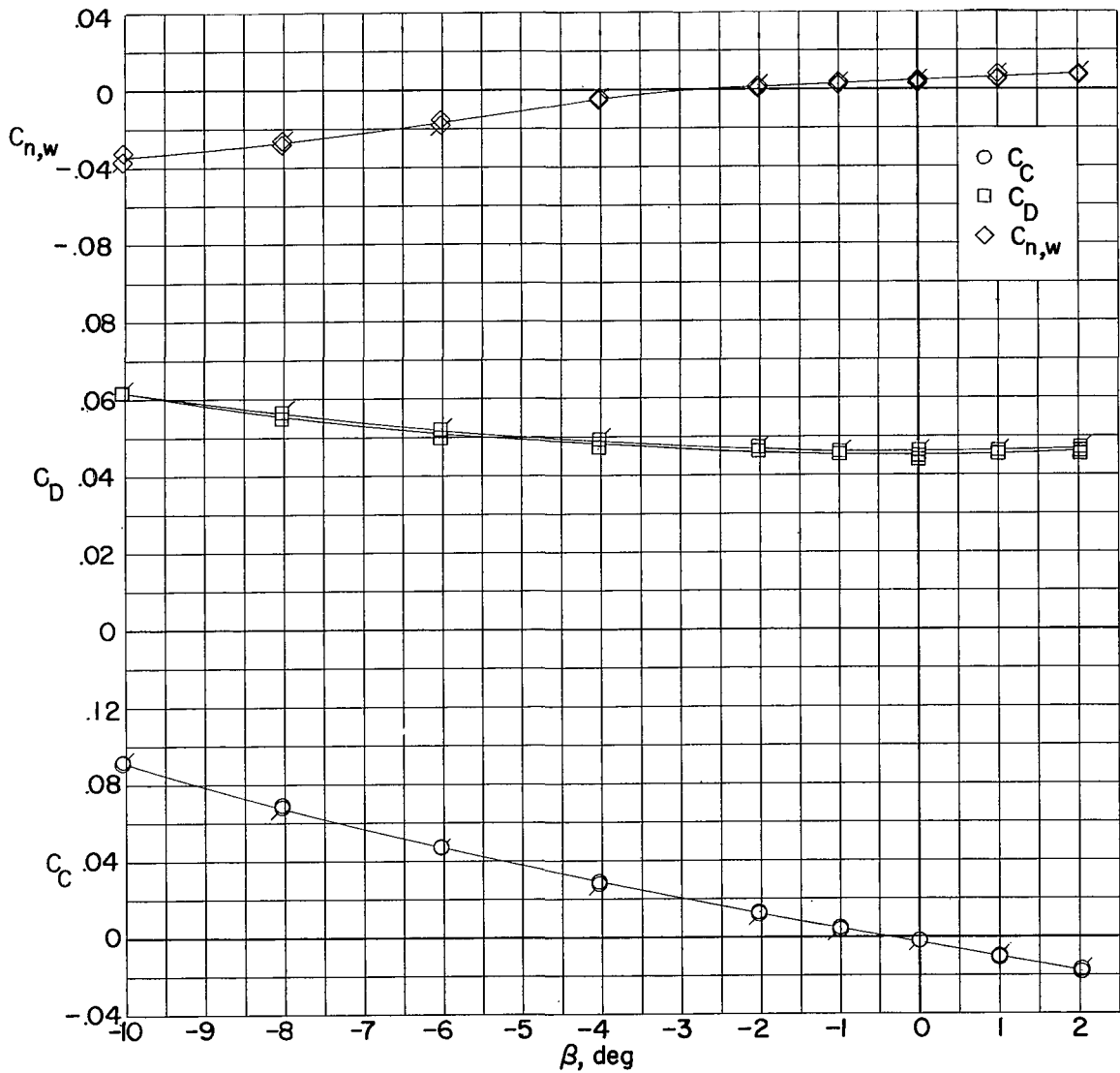
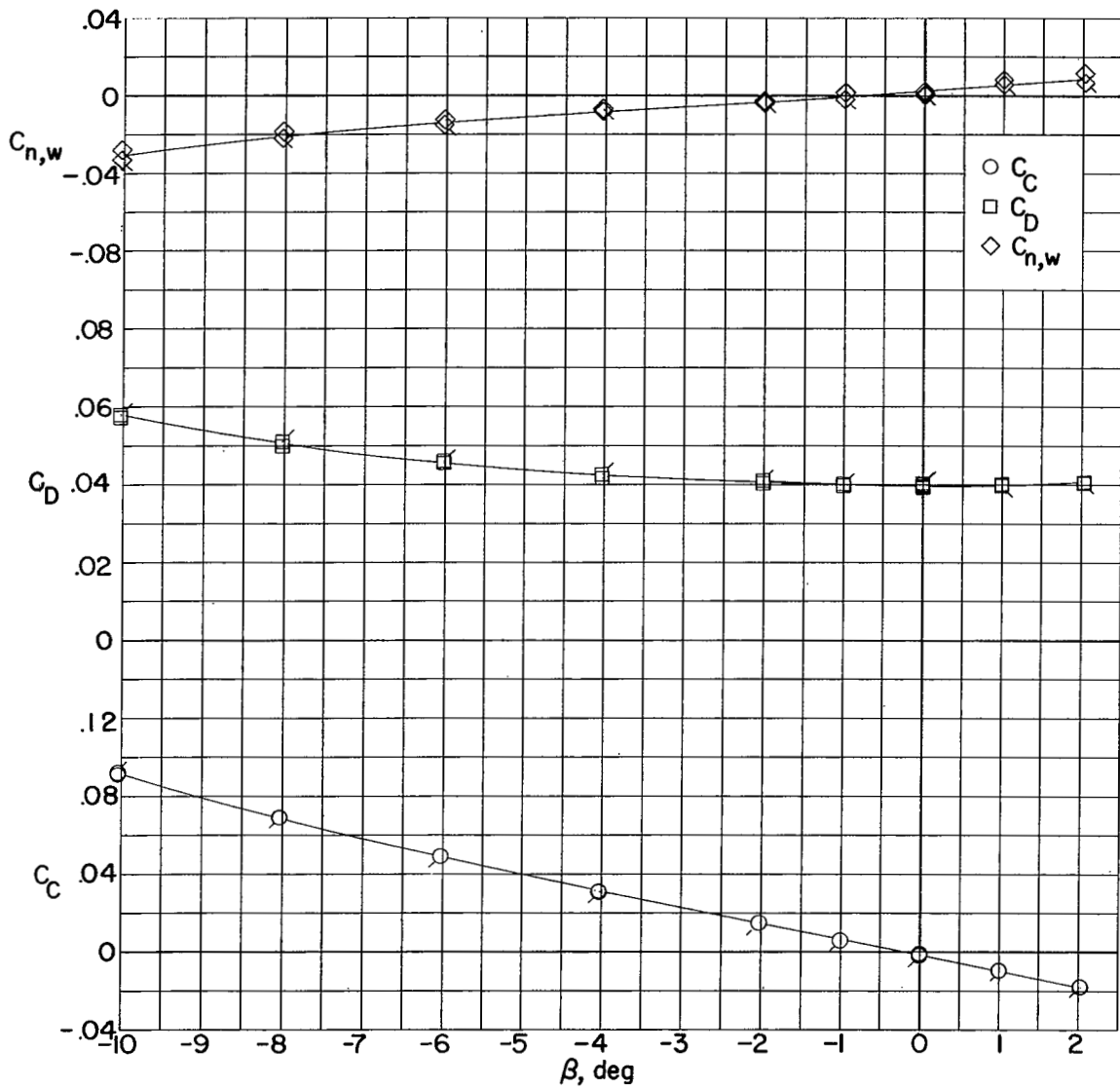
(a)  $M_\infty = 1.94$ .

Figure 7.- Measured aerodynamic characteristics of model 1 low-tail configuration in sideslip. (Flagged symbols indicate models with transition strips.)



(b)  $M_\infty = 2.40$ .

Figure 7.- Concluded.

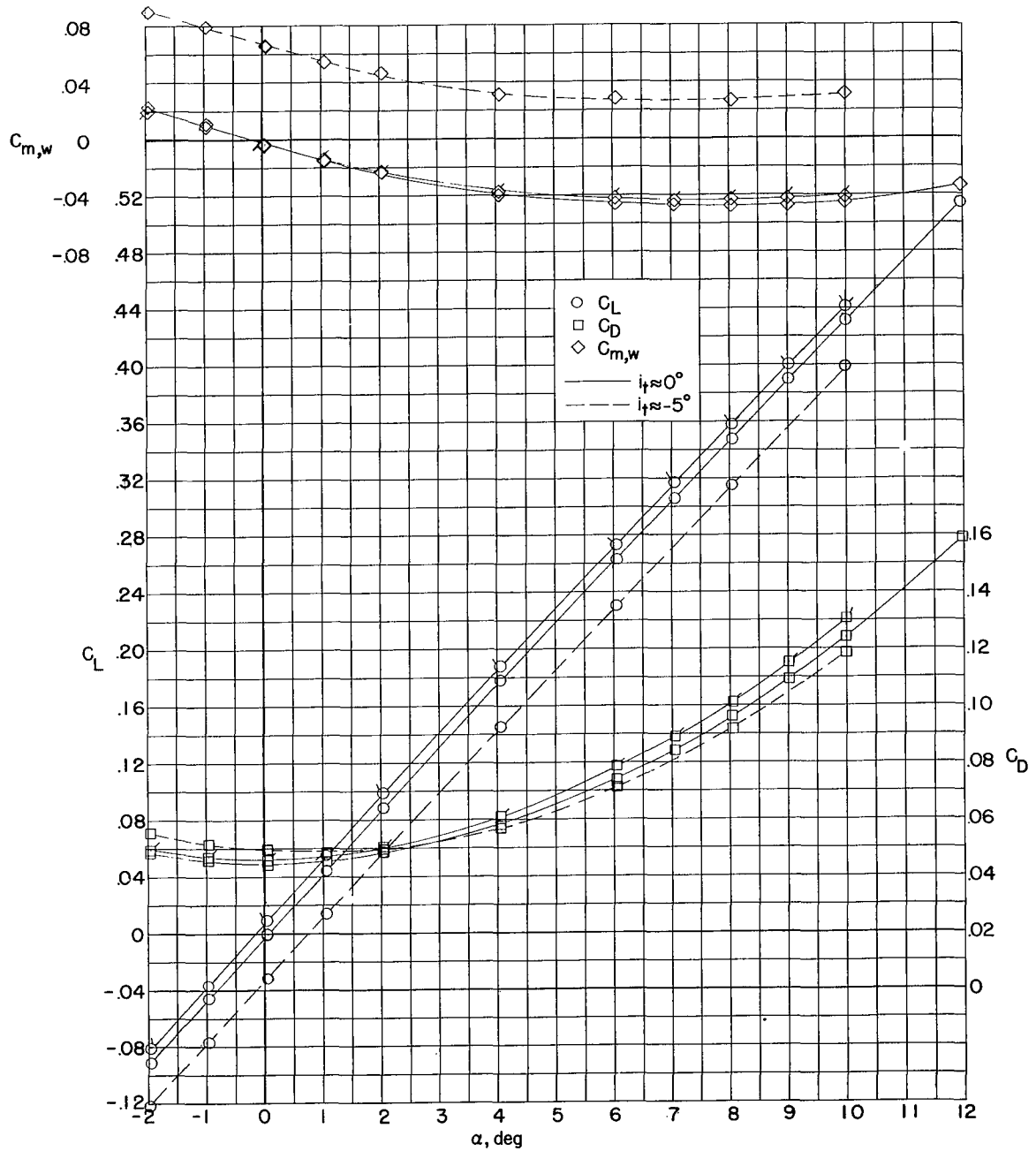
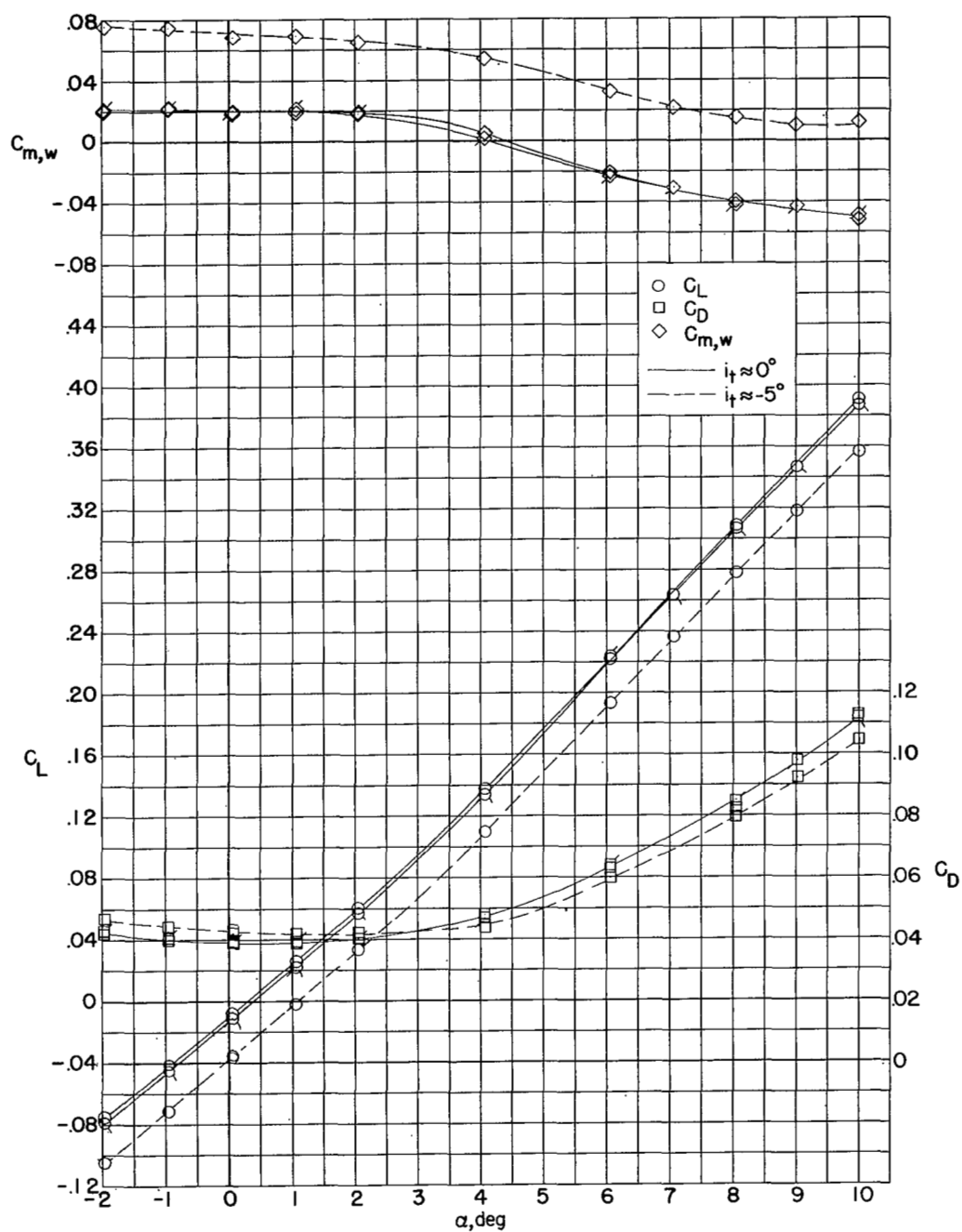
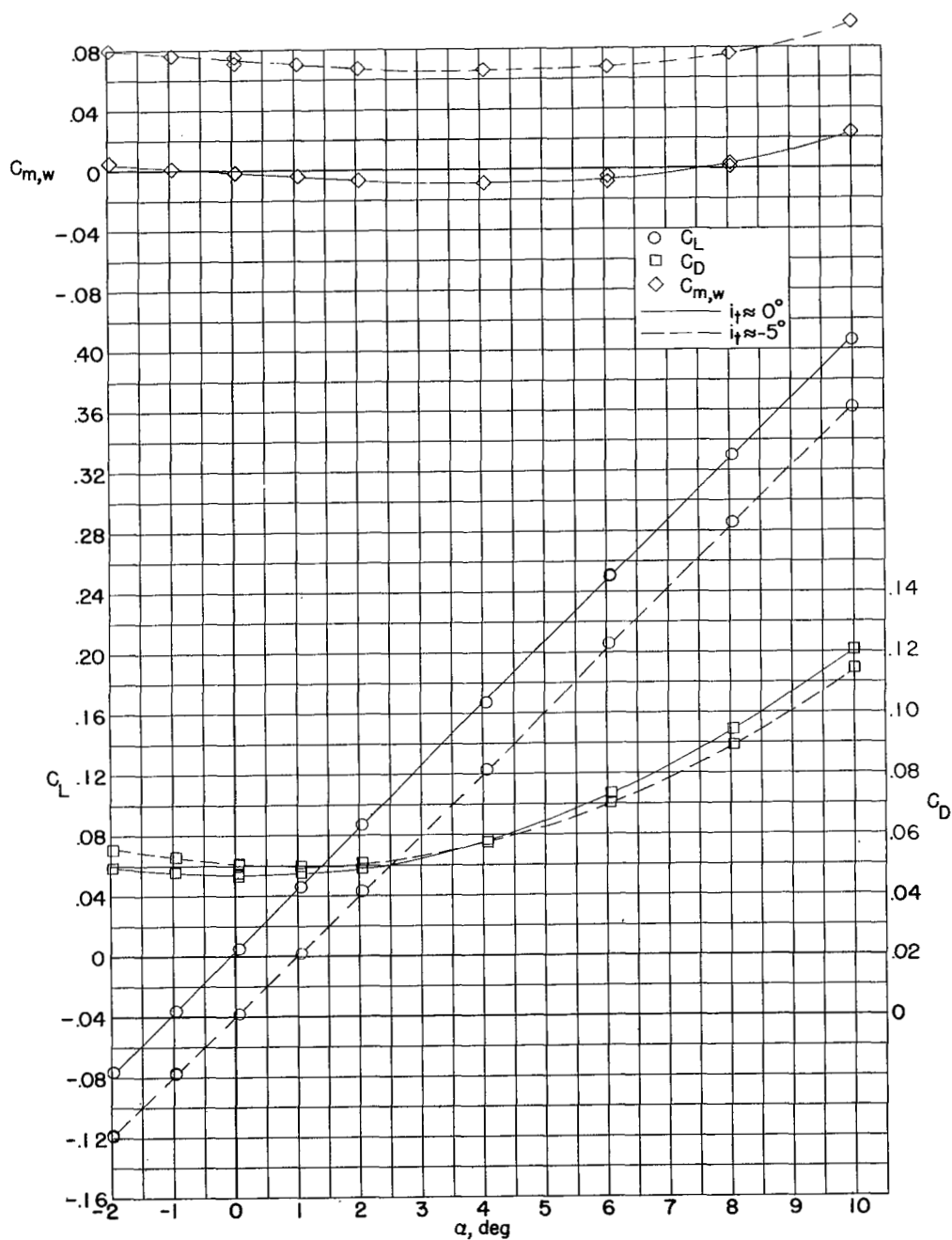
(a)  $M_\infty = 1.94$ .

Figure 8.- Measured aerodynamic characteristics of model 2 high-tail configuration in pitch. (Flagged symbols indicate model with transition strips.)



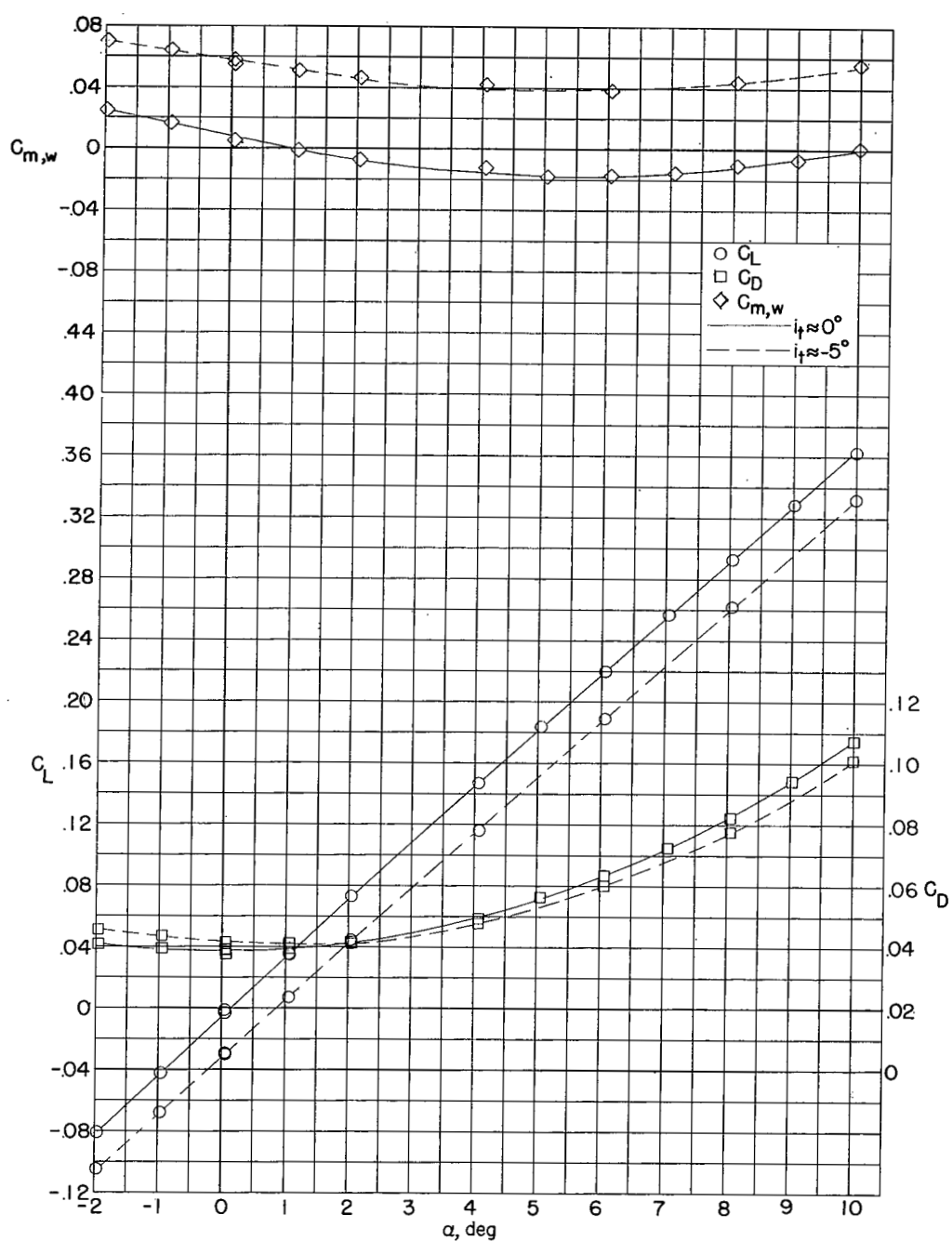
(b)  $M_\infty = 2.40$ .

Figure 8.- Concluded.



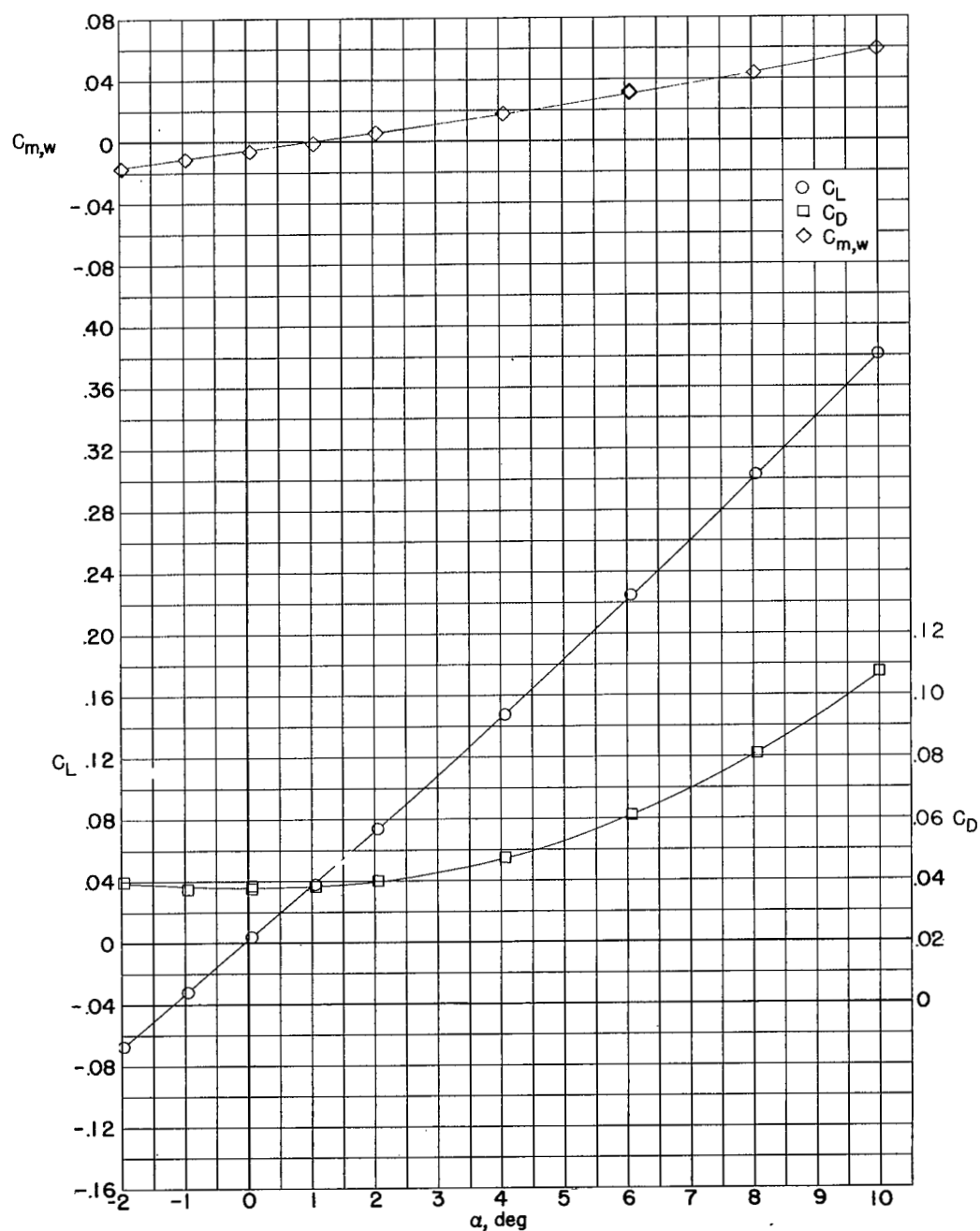
(a)  $M_\infty = 1.94$ .

Figure 9.- Measured aerodynamic characteristics of model 2 low-tail configuration in pitch.



(b)  $M_\infty = 2.40$ .

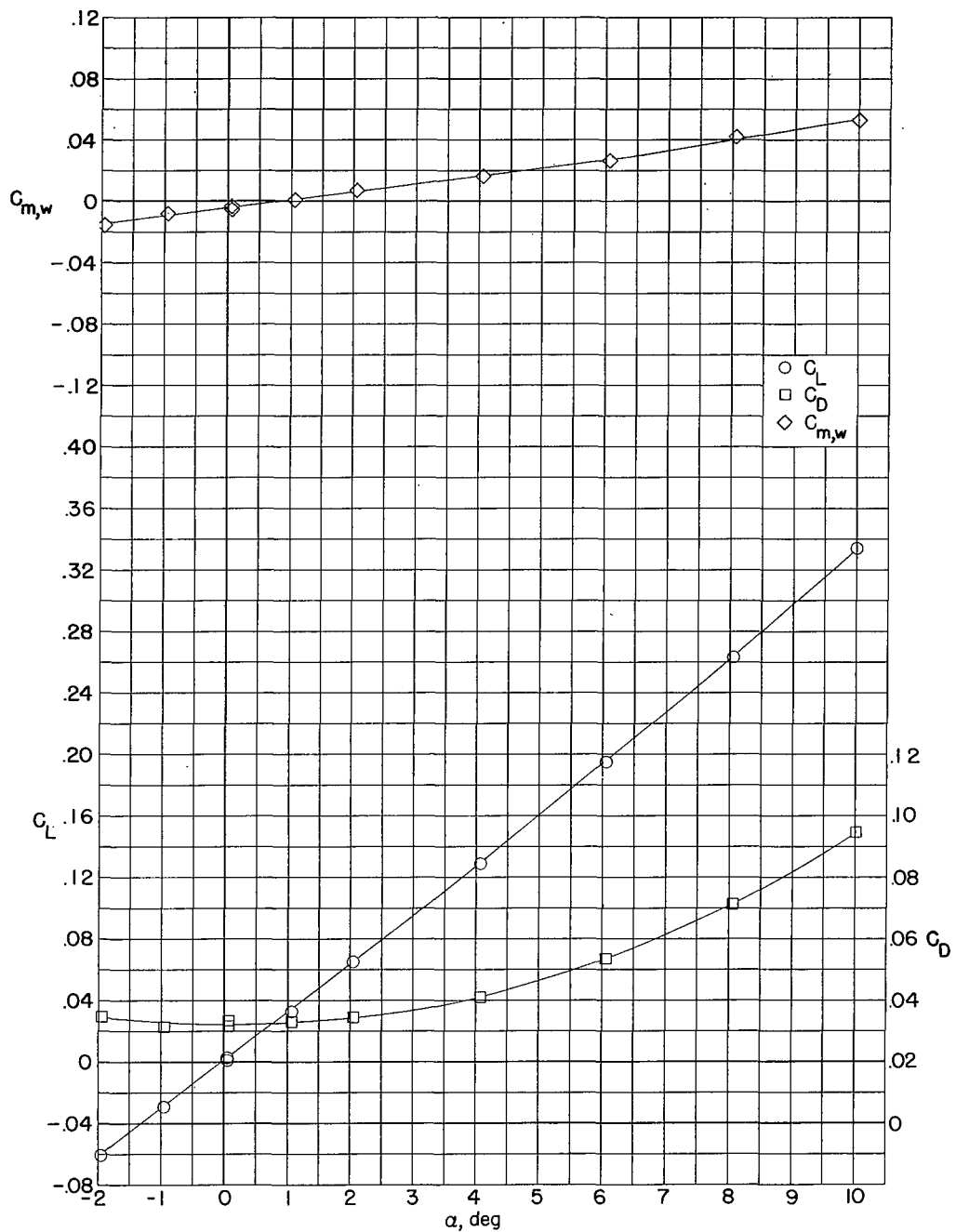
Figure 9.- Concluded.



(a)  $M_\infty = 1.94$ .

Figure 10.- Measured aerodynamic characteristics of model 2 in pitch.  
No horizontal tail.





(b)  $M_\infty = 2.40$ .

Figure 10.- Concluded.

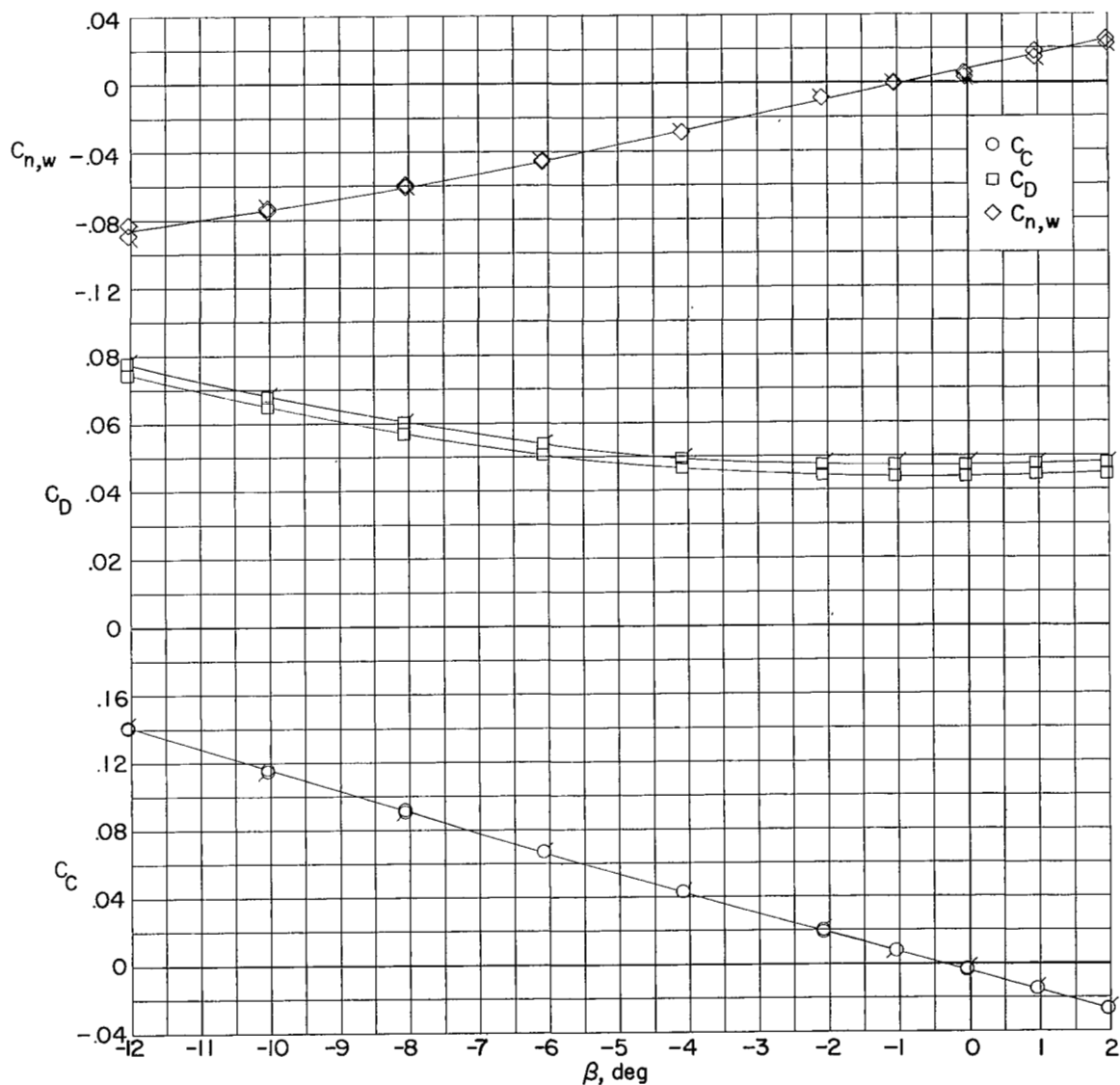
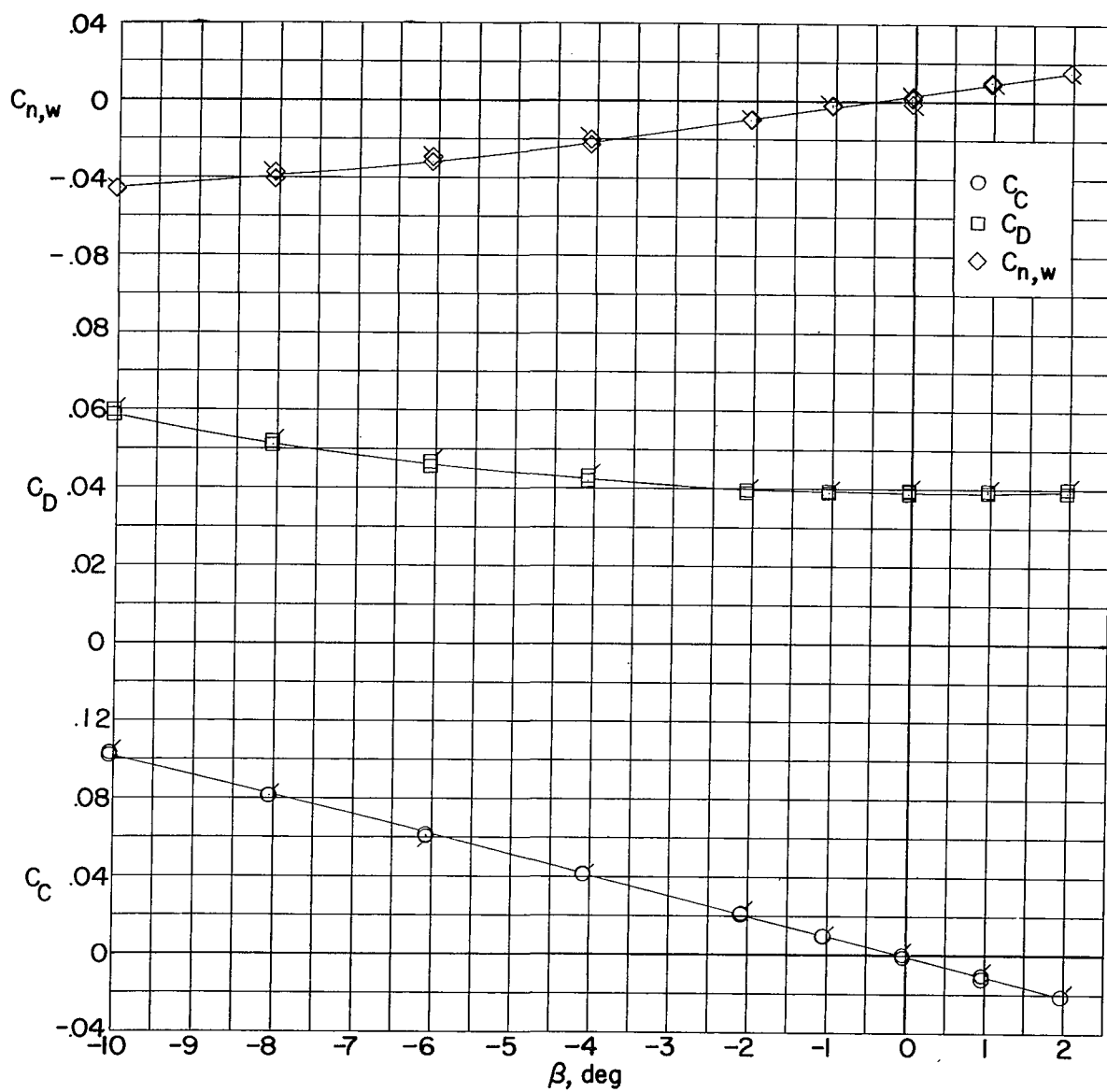
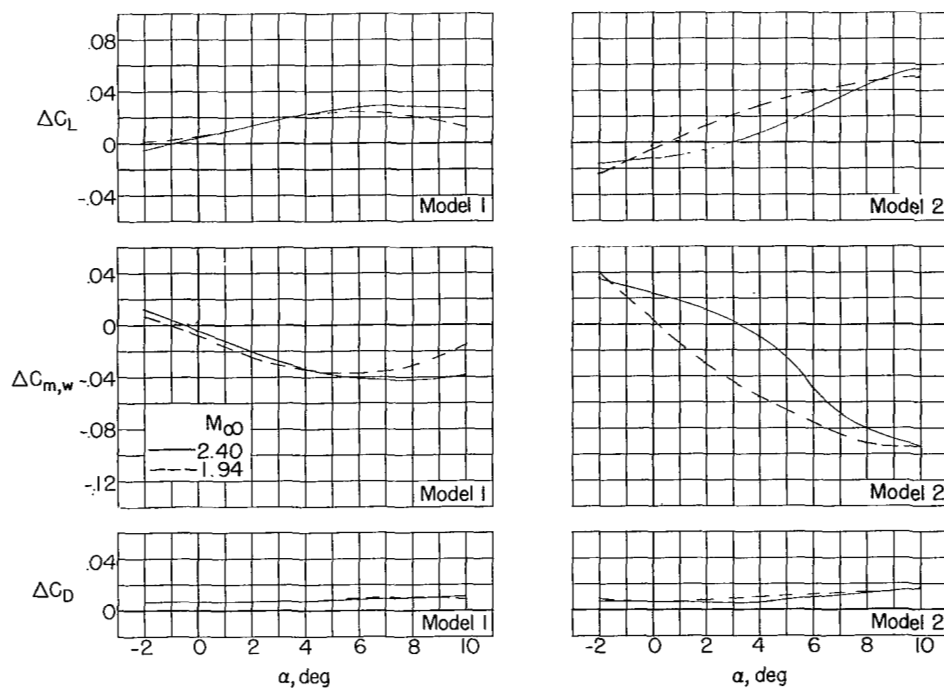
(a)  $M_\infty = 1.94$ .

Figure 11.- Measured aerodynamic characteristics of model 2 high-tail configuration in sideslip. (Flagged symbols indicate model with transition strips.)

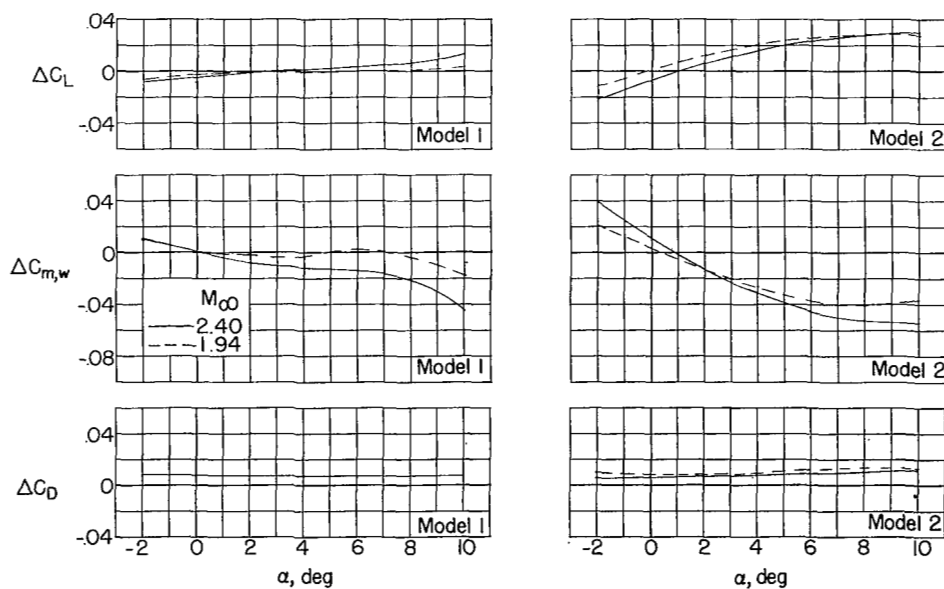


(b)  $M_\infty = 2.40$ .

Figure 11.- Concluded.

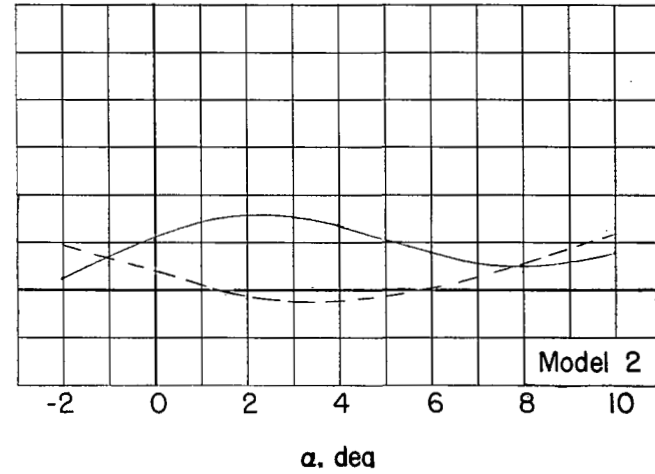
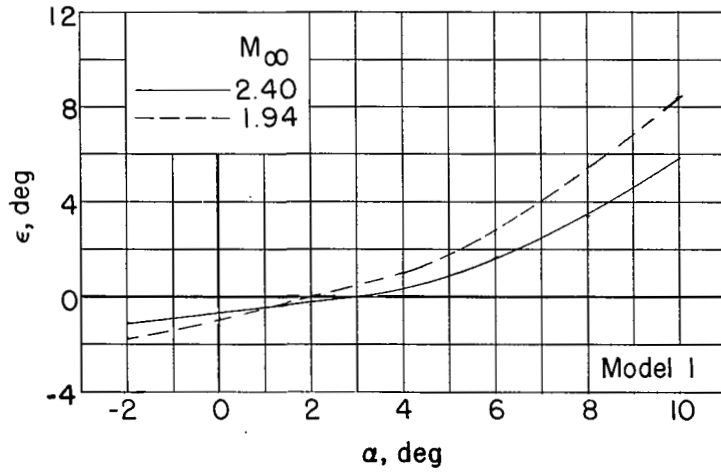


(a) High-tail configurations.

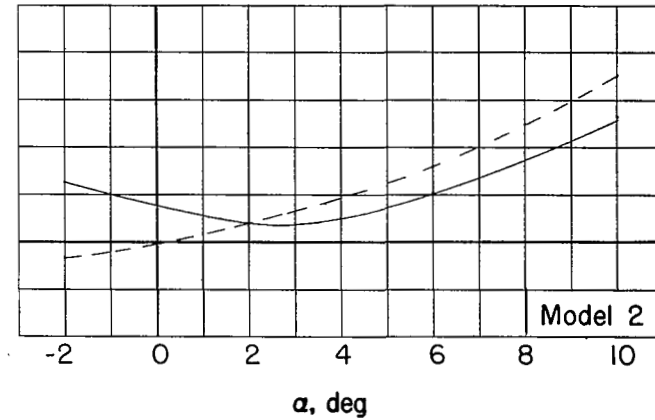
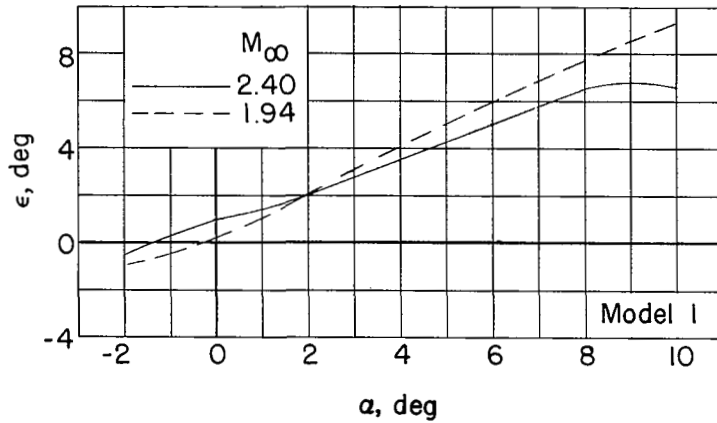


(b) Low-tail configurations.

Figure 12.- Incremental results as a result of adding the horizontal tail at  $i_t \approx 0^\circ$ .

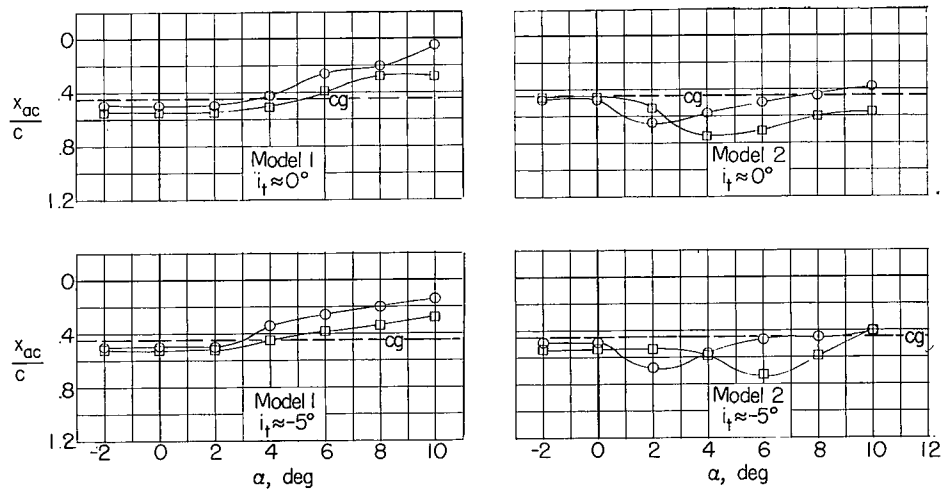


(a) High-tail configurations.

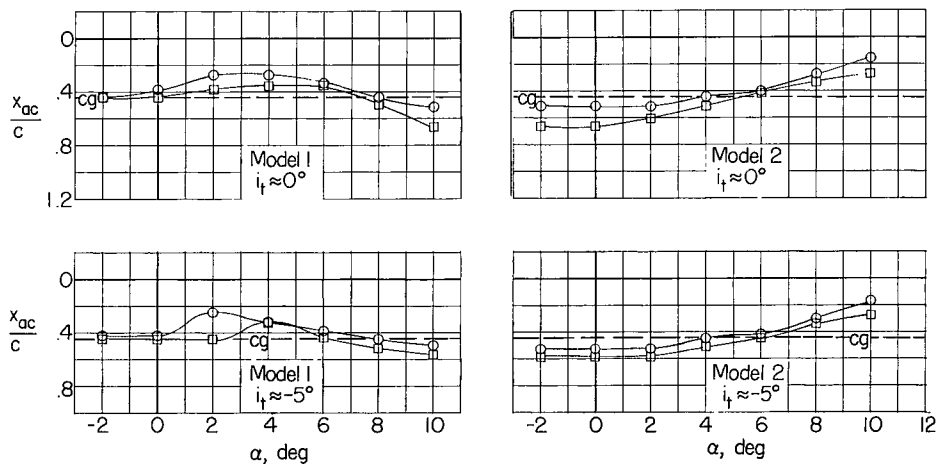


(b) Low-tail configurations.

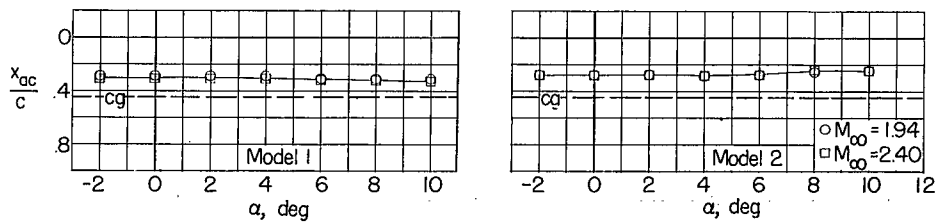
Figure 13.- Variation of effective downwash angle with angle of attack.



(a) High-tail configurations.

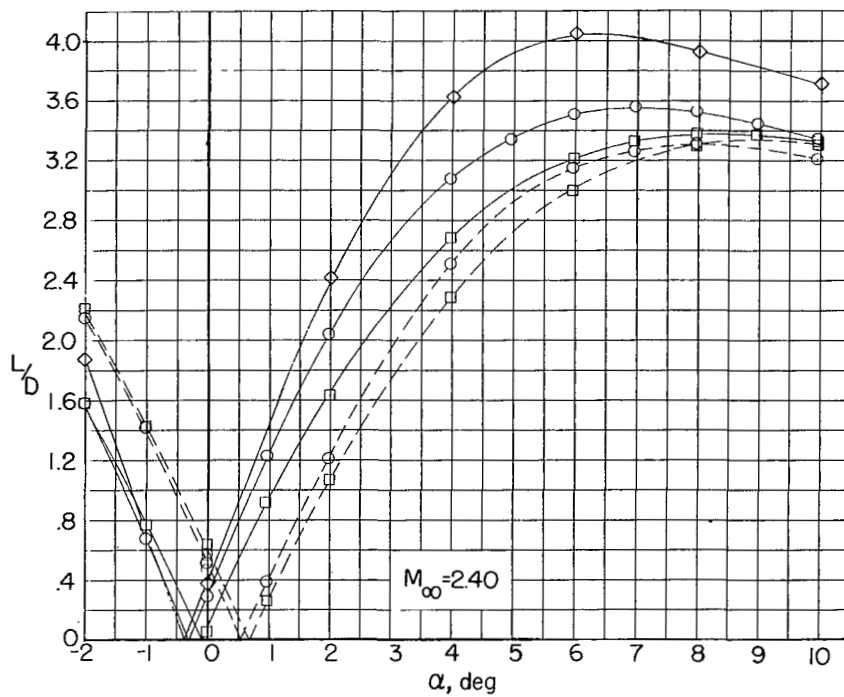
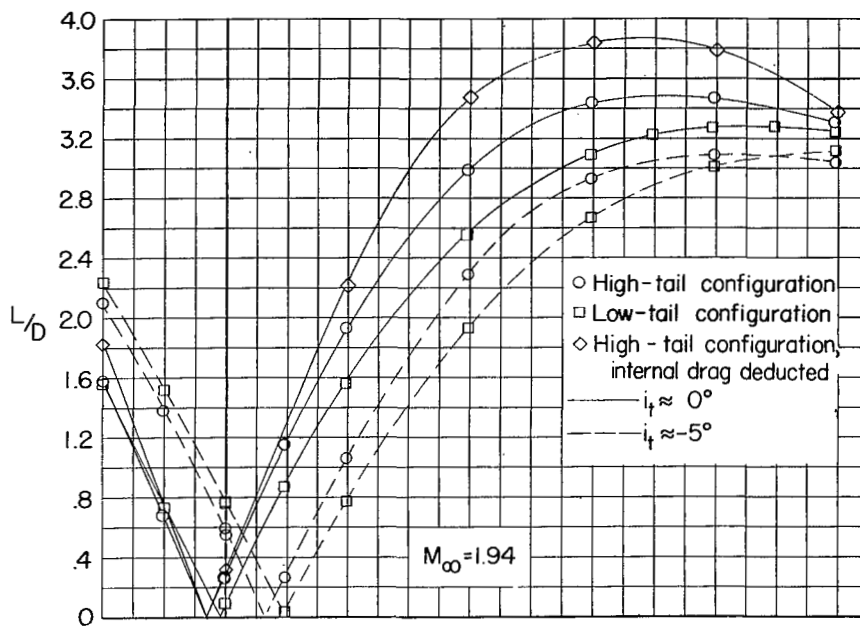


(b) Low-tail configurations.



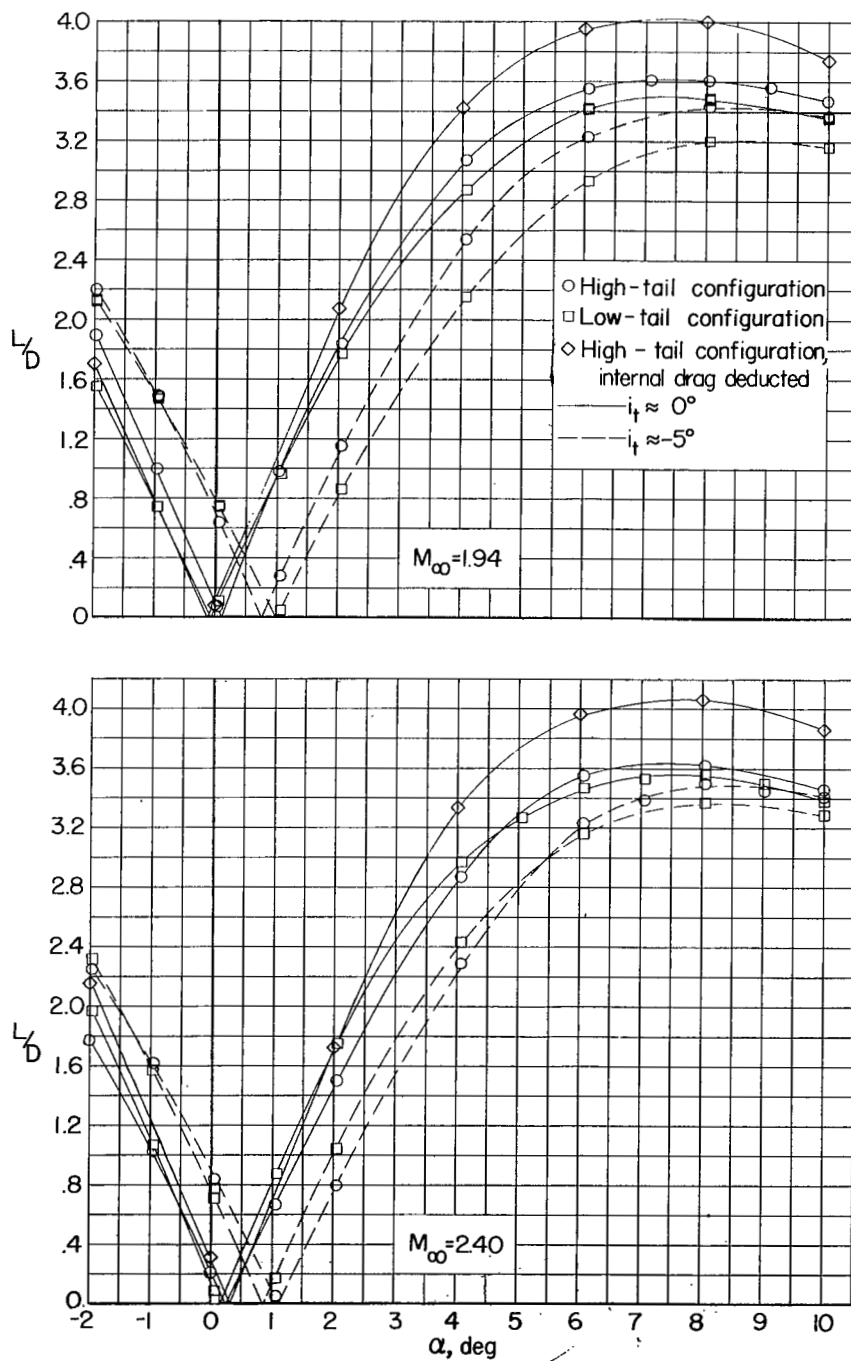
(c) No horizontal tail.

Figure 14.- Aerodynamic-center locations in pitch referenced to wing leading edge.



(a) Model 1.

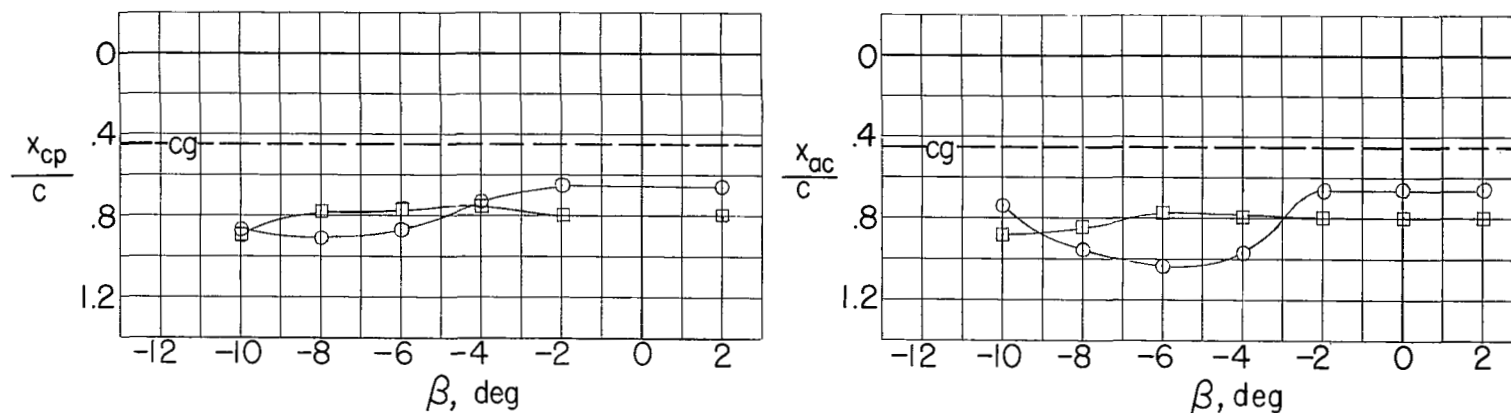
Figure 15.- Lift-drag ratios.



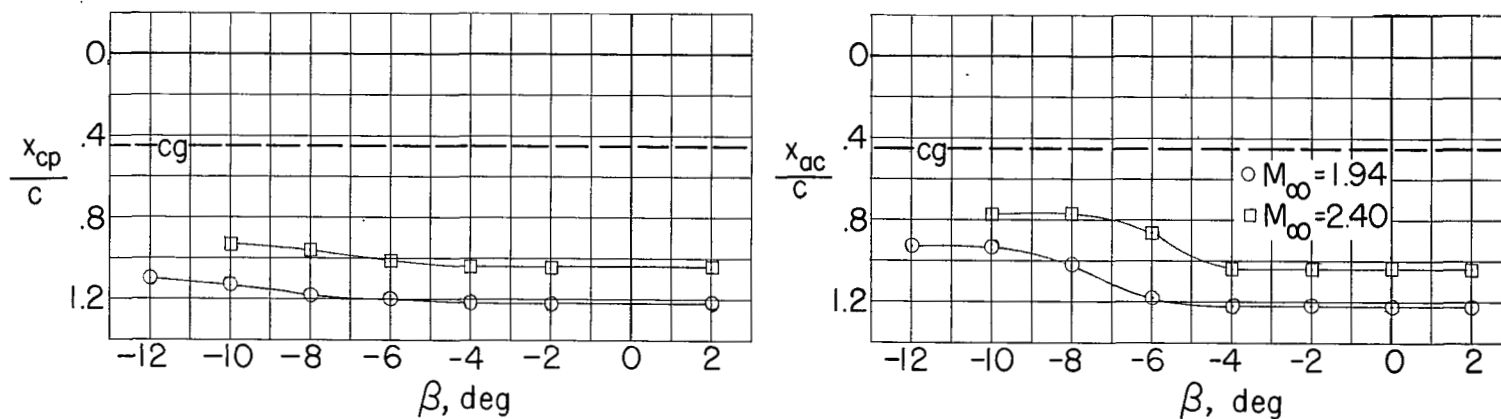
(b) Model 2.

Figure 15.- Concluded.



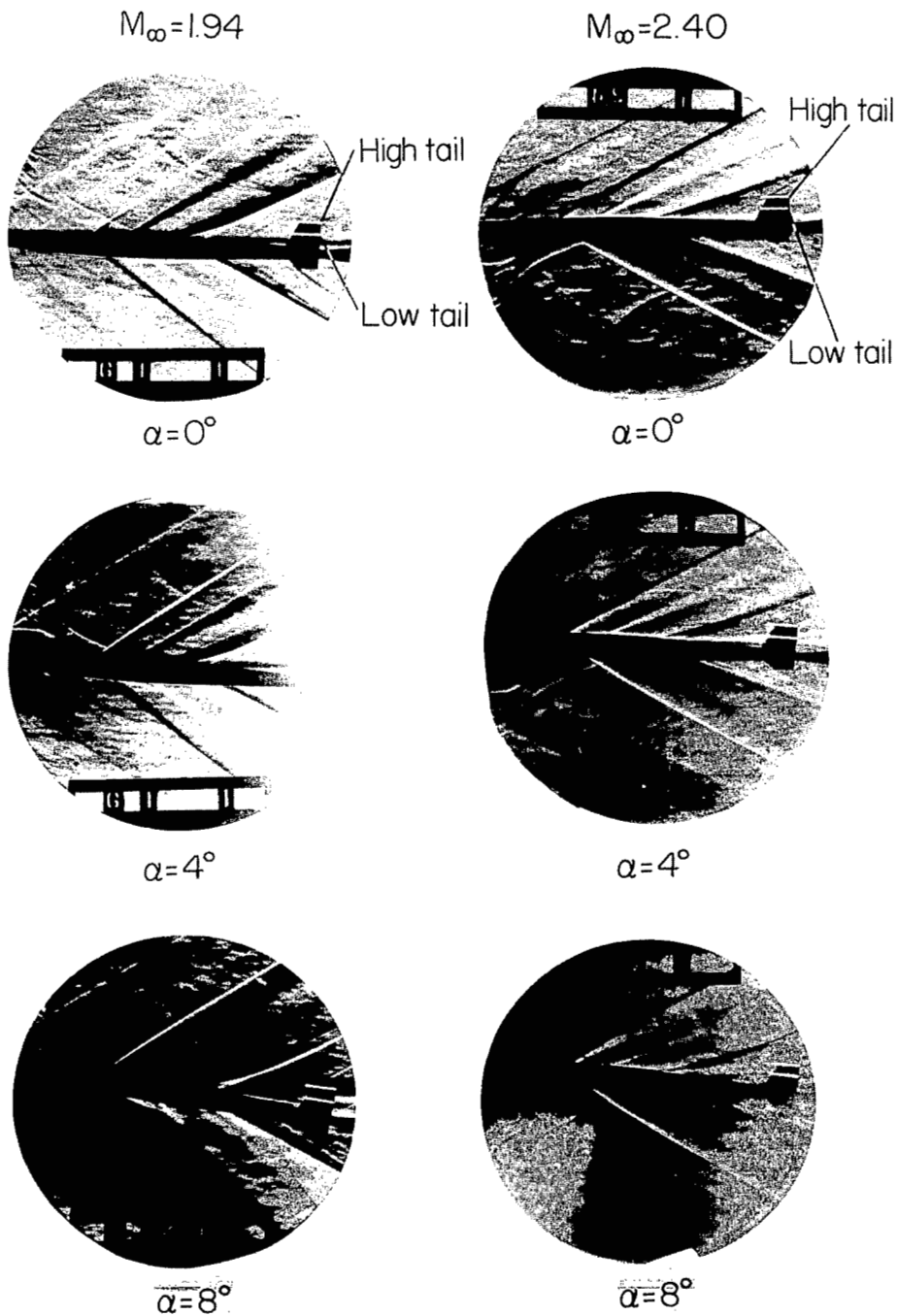


(a) Model 1, high tail.



(b) Model 2, low tail.

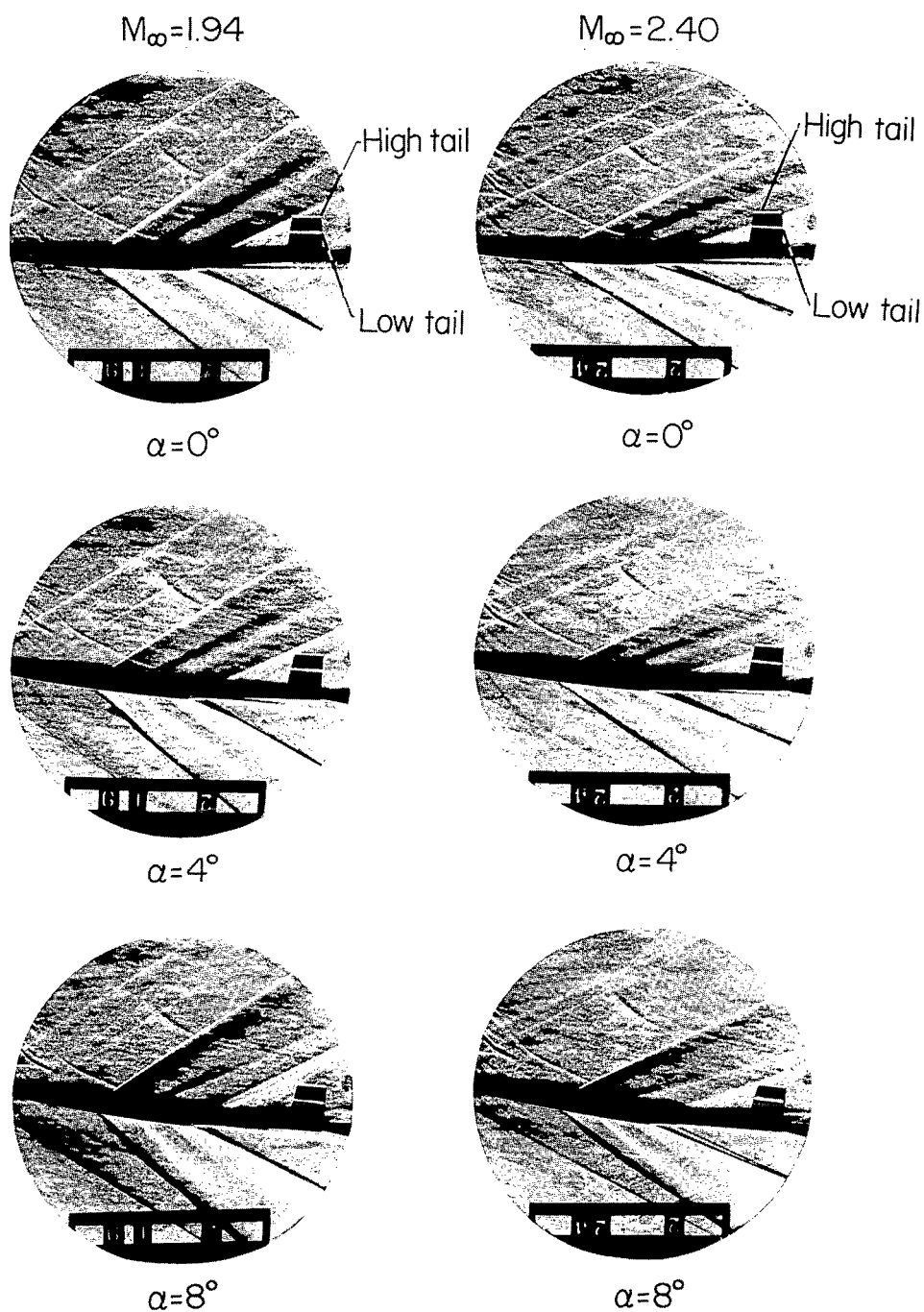
Figure 16.- Center-of-pressure and aerodynamic-center locations in sideslip.



(a) Model 1.

L-95779

Figure 17.- Schlieren photographs. (No transition strips installed.)



(b) Model 2.

L-95780

Figure 17.- Concluded.

NASA Technical Library



3 1176 01437 7445

[REDACTED]